Master's Thesis
Master's Degree Programme in Space Sciences

THE EFFECT OF THERMAL INSTABILITY ON THE DEVELOPMENT OF THE GALACTIC DYNAMO

Elizabeth Melanie Cole

May 2011

Supervisor: Maarit Mantere

Reviewers: Hannu Koskinen
Maarit Mantere

DEPARTMENT OF PHYSICS
UNIVERSITY OF HELSINKI

P.O.Box 64 (Gustaf Hällströmin katu 2)
FI-00014 University of Helsinki

HELSINGIN YLIOPISTO – HELSINGFORS UNIVERSITET – UNIVERSITY OF HELSINKI

Tiedekunta/Osasto – Fakultet/Sektion – Faculty/Section	Laitos – Institution – Department	
Science	Physics	
Tekijä – Författare – Author		
Elizabeth Melanie Cole		
Työn nimi – Arbetets titel – Title		
The Effect of Thermal Instability on the Development of the Galactic Dynamo		
Oppiaine – Läroämne – Subject		
Astronomy		
Työn laji – Arbetets art – Level	Aika – Datum – Month and year	Sivumäärä – Sidoantal – Number of pages
Pro Gradu	May 2011	56

Tiivistelmä – Referat – Abstract

Thermal instability (hereafter TI) is investigated in numerical simulations to determine its effect on the growth and efficiency of the dynamo processes. The setup used is a three-dimensional periodic cube of a size several times the correlation length of the interstellar turbulence. The simulations are designed to model the interstellar medium without any shear and rotation, to isolate the effect of TI. Hydrodynamical and nonhelical simulations are run for comparison to determine the effects the magnetic field has upon the gas itself. Turbulence is simulated by external helical forcing of varying strength, which is known to create a large-scale dynamo of alpha squared -type. The nonhelical cases are also explored in an attempt to create a small-scale dynamo at high Rm, but no dynamo action could be detected in the range of Rm ~ 30 -150. The hydrodynamical simulations reproduce the tendency of the gas to separate into two phases if an unstable cooling function is present. The critical magnetic Reynolds number of the large-scale dynamo was observed to be almost twice as large for the unstable versus stable cooling function, indicating that the dynamo is harder to excite when TI is present. The efficiency of the dynamo as measured by the ratio of magnetic to kinetic energy was found to increase for the unstable case at higher forcing. The results of the runs from this thesis are part of a larger project studying dynamo action in interstellar flows.

Avainsanat – Nyckelord – Keywords

thermal instability --- dynamo theory -- interstellar turbulence --- galactic dynamos

Säilytyspaikka – Förvaringställe – Where deposited

Physics Department

Muita tietoja – Övriga uppgifter – Additional information

Abstract

Thermal instability (hereafter TI) is investigated in numerical simulations to determine its effect on the growth and efficiency of the dynamo processes. The setup used is a three-dimensional periodic cube of a size several times the correlation length of the interstellar turbulence. The simulations are designed to model the interstellar medium without any shear or rotation, to isolate the effect of TI. Hydrodynamical and nonhelical simulations are run for comparison to determine the effects the magnetic field has upon the gas itself. Turbulence is simulated by external helical forcing of varying strength, which is known to create a large-scale dynamo of α^2-type. The nonhelical cases are also explored in an attempt to create a small-scale dynamo at high Rm, but no dynamo action could be detected in the range of $Rm \approx 30 - 150$. The hydrodynamical simulations reproduce the tendency of the gas to separate into two phases if an unstable cooling function is present. The critical magnetic Reynolds number of the large-scale dynamo was observed to be almost twice as large for the unstable versus stable cooling function, indicating that the dynamo is harder to excite when TI is present. The efficiency of the dynamo as measured by the ratio of magnetic to kinetic energy was found to increase for the unstable case at higher forcing. The results of the runs from this thesis are part of a larger project studying dynamo action in interstellar flows.

Awknowledgements

I'd first like to thank my advisor, Dr. Maarit Mantere, for her endless support, patience, and knowledge. I could not have asked for a better advisor to guide me through the work.

I would also like to thank Prof. Hannu Koskinen for his help in providing insight into my thesis, and his encouragement to keep up with my work.

And I'd like to thank my family and friends for supporting me, for giving me the motivation to even begin the work and see it through to the end.

Contents

1

Introduction

1.1 Magnetohydrodynamics and Plasma

Plasma is often referred to as the fourth state of matter, separate from a solid, liquid, or gas. When a gas is heated enough to split the electrons and the ions so that they are free to move about and form currents, it is considered a plasma.

Magnetohydrodynamics (hereafter MHD) is the study of plasmas at the macroscopic level using the magnetic field as a reference point, combining electrodynamics with hydrodynamical equations of fluids. The material can be treated as a fluid, i.e., a continuous medium, if the average mean free path of the particles is much smaller than the length scale of the system. The most important equation is the induction equation, derived from Maxwell's Laws:

$$\frac{\partial \mathbf{B}}{\partial t} = \nabla \times (\mathbf{U} \times \mathbf{B}) + \eta \nabla^2 \mathbf{B}. \tag{1.1}$$

The first term on the right hand side is the advection term and the second is the diffusion term. The ratio of these gives the magnetic Reynolds number, a dimensionless quantity describing the ratio of advection to diffusion, i.e., the ability of the fluid to amplify the field with respect to diffusive effects.

$$Rm = \frac{L_o V_o}{\eta}, \tag{1.2}$$

where L_o and V_o are the scale length and typical velocity respectively. A low magnetic Reynolds number indicates a field that diffuses and changes on a time scale

$$\tau_d = \frac{L_o}{\eta}. \tag{1.3}$$

A very high magnetic Reynolds number gives the frozen-in condition where the diffusion is much less than the advection and essentially drops out of (1.1) to give

$$\frac{\partial \mathbf{B}}{\partial t} = \nabla \times (\mathbf{U} \times \mathbf{B}) \,. \tag{1.4}$$

The magnetic flux is then conserved, leading to a visualization trick where the magnetic field can be represented as a collection of flux tubes where two particles along a particular magnetic line share a magnetic line over time. The magnetic field moves with the plasma; hence it is said to be frozen-in. It should be noted that such magnetic lines are not physical structures. The magnetic Reynolds number is useful in determining the type of plasma being investigated and the expected properties, as well as whether the ideal form of the MHD equations (1.4) is valid.

The other extreme is highly diffusive plasma, where Rm is very small. The induction equation becomes

$$\frac{\partial \mathbf{B}}{\partial t} = \eta \nabla^2 \mathbf{B}. \tag{1.5}$$

High diffusion plays an important role in phenomena such as reconnection, where oppositely oriented magnetic fields connect and change into a new, more complex field.

1.2 Thermal Instability

Thermal instability was first proposed by Parker (1953) to explain observed properties of solar prominences. He theorized that a gas at near equilibrium could condense if the radiative losses increase with the decreasing temperature of the gas packet so that a cooler region continues to rapidly drop in temperature until it is well below the initial equilibrium value. The result is a condensation that is not due to gravity, and the gas tends to separate into two phases, one warm and diffuse and the other cold and dense. The solutions to the dispersion relation that resulted in this thermal instability were more thoroughly explored by Field (1965).

The basic idea is as follows: assume a medium such as the interstellar gas, of constant density ρ_o and temperature T_o. The generalized heat loss function is then

$$\mathcal{L}(\rho_o, T_o) = 0, \tag{1.6}$$

where $\mathcal{L}$ is the energy loss minus the energy gains of the system. The gas is then perturbed such that some thermodynamic quantity A is held constant. Rewriting the

change of entropy $\Delta s = q/T$ into the form

$$\Delta \mathcal{L} dT = -T d(\Delta s) \tag{1.7}$$

gives a general instability criterion

$$\left(\frac{\partial \mathcal{L}}{\partial s}\right)_A > 0, \tag{1.8}$$

is found, where A is whatever thermodynamic quantity was selected to be constant. The sign convention used is such that if the mathematical statement is true, then the system is unstable.

For isochoric perturbations the density is presumed constant (i.e., $Tds = C_v dT$). The instability occurs if

$$\left(\frac{\partial \mathcal{L}}{\partial T}\right)_\rho < 0. \tag{1.9}$$

However, small perturbations in pressure would quickly destroy the constant density requirement, making this a less physically real criterion to maintain. This was the criterion initially proposed by Parker in 1953. Although this is interesting from a theoretical point of view, other criteria must be used for physical cases.

A more realistic approach is to use isobaric perturbations, i.e., constant pressure, so that $Tds = C_p dT$. Using (1.8) where $A = p$ gives an instability criterion

$$\left(\frac{\partial \mathcal{L}}{\partial T}\right)_p = \left(\frac{\partial \mathcal{L}}{\partial T}\right)_\rho - \frac{\rho_o}{T_o}\left(\frac{\partial \mathcal{L}}{\partial \rho}\right)_T < 0. \tag{1.10}$$

The isobaric criterion has the advantage over the isochoric in that small density perturbations do not destroy the condition and thus can be used as the governing criterion. It has an advantage in astrophysical applications due to the tendency of interstellar material to have a positive heat derivative with respect to ρ, thus creating a growing instability over time.

A third condition is the isentropic condition where entropy is the quantity held constant,

$$\left(\frac{\partial \mathcal{L}}{\partial T}\right)_S = \left(\frac{\partial \mathcal{L}}{\partial T}\right)_\rho + \frac{1}{\gamma - 1}\frac{\rho_o}{T_o}\left(\frac{\partial \mathcal{L}}{\partial \rho}\right)_T < 0. \tag{1.11}$$

It can be seen from the equation that, unlike for the isobaric criterion, a positive derivative with respect to ρ will stabilize the matter. It will be shown that if the

condition for either the isochoric or isentropic instability is satisfied, then the isobaric condition is also satisfied, making the isobaric condition the most limiting one.

To demonstrate this, take a compressible perfect gas. The governing hydrodynamical equations of state can then be written in the following forms:

$$\frac{D\ln\rho}{Dt} = -\nabla\cdot\mathbf{u}, \tag{1.12}$$

$$\rho\frac{D\mathbf{u}}{Dt} = -\nabla p + \nabla\cdot(2\nu\rho\mathbf{S}), \tag{1.13}$$

and

$$T\frac{Ds}{Dt} = 2\nu\mathbf{S}^2 + \frac{1}{\rho}\nabla\cdot(c_p\rho\chi\nabla T) - \mathcal{L}, \tag{1.14}$$

where $\mathbf{u}$ is the velocity, ρ is the density, $S_{ij} = \frac{1}{2}(u_{i,j} + u_{j,i}) - \frac{1}{3}\delta_{ij}\nabla\cdot\mathbf{u}$ is the traceless rate-of-strain tensor, s is the specific entropy, ν is the kinematic viscosity, χ is the thermal diffusivity, and $\mathcal{L}$ is the same generalized net heating function as in (1.6). D/Dt is the Lagrangian derivative where $D/Dt = \partial/\partial t + \mathbf{u}\cdot\nabla$. (1.12) is the continuity equation, (1.13) is the equation of motion, and (1.14) is the entropy equation. To close the system of equations, i.e., to relate density, pressure, and temperature, the ideal gas law is used:

$$p = \frac{R}{\mu}\rho T \tag{1.15}$$

and

$$s = c_v\ln p - c_p\ln\rho + s_o, \tag{1.16}$$

where R is the ideal gas constant, μ in this case is the mean molecular weight such that that $R/\mu = c_p - c_v$, $\gamma = c_p/c_v = 5/3$ for an ideal gas, s_o is a constant, and the speed of sound is $c_s^2 = \gamma RT/\mu$. A typical value for μ in interstellar applications is 0.62. The heat equation $\mathcal{L}$ is given the form

$$\mathcal{L} = \rho\Lambda - \Gamma, \tag{1.17}$$

where Γ is a constant and Λ is a cooling function dependent on temperature. A simplified power law can be fit over intervals of temperature T to give an equation of the form

$$\Lambda(T) = CT^{\beta}, \tag{1.18}$$

where C and β are constants over one interval. Taking the derivative gives

$$\beta = \frac{d(\ln \Lambda)}{d(\ln T)}, \tag{1.19}$$

into which (1.9), (1.10), and (1.11) can now be inserted, giving

$$\beta < 0, \qquad \text{(isochoric)} \tag{1.20}$$

$$\beta < 1, \qquad \text{(isobaric)} \tag{1.21}$$

and

$$\beta < \frac{1}{1-\gamma} = -\frac{3}{2} \qquad \text{for } \gamma = 5/3, \quad \text{(isentropic)} \tag{1.22}$$

respectively. The isobaric mode is of the most interest, as it is the most restrictive of all the conditions for instability, and an isochoric or isentropic instability automatically satisfies the isobaric condition. If (1.18) is fitted piecewise as a cooling function, instabilities can occur over any temperature interval where $\beta < 1$. As a consequence, any cooling function with a segment that is unstable in a certain temperature range will create two stable phases of matter, one cool and dense and the other hot and diffuse. It is one proposed mechanism that can create the observed multiphase property of interstellar material not adequately described by gravity.

1.3 The Interstellar Medium

A spiral galaxy typically consists of a bulge, a disk, and a halo. The classification is based on the size of the bulge and the extent to which the arms have a bar.

The properties of the gas (and the star types) depend primarily on location. The spiral arms located in the disk are of particular interest because of their observable structure, and indeed, most magnetic fields appear to correspond with the arms to some extent. More specific examples are given later. There are magnetic interactions that are observed in the halo itself, so any magnetic field is a three-dimensional structure. However, for the purpose of this thesis the area of concern is the thin disk. The thin disk normally contains cold atomic gas, warm atomic gas, and hot ionized gas from supernovae (see Table 1.1). If the effects of supernovae are not taken into consideration, this leaves just two observed phases in the interstellar medium in the thin disk. Warm ionized gas is found in the thick disk, and molecular clouds are typically star formation regions and much denser than most of the ISM.

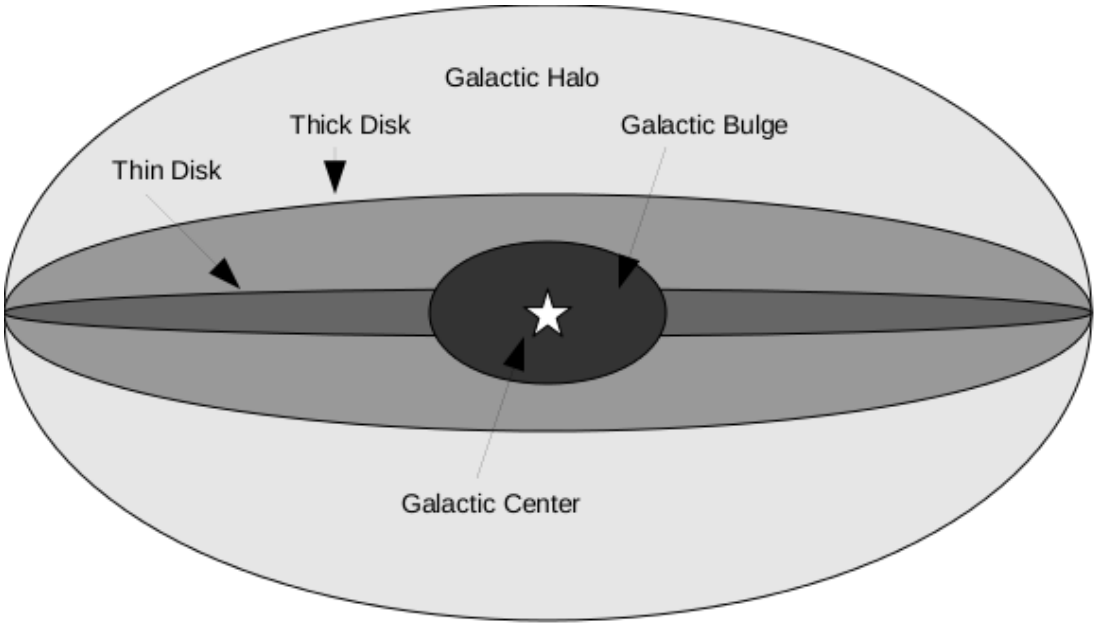

Figure 1.1: Galaxy Structure - Basic structure of a galaxy viewed from the edge. Depending on the location, the gas has very different properties.

Componenent	**T** [K]	**n** [cm^{-3}]	Scale Height [pc]
Molecular	10-20	$10^2 - 10^6$	70
Cold Atomic	50-100	20-50	100-300
Warm Atomic	6000-10000	0.2-0.5	300-400
Warm Ionized	∼8000	0.2-0.5	1000
Hot Ionized	$\sim 10^6$	∼0.0065	1000-3000

Table 1.1: Properties of various gases in the interstellar medium. Values are taken from Ferriere (2001).

The tendency of the gas to separate into these different phases is theorized to be due to a thermally unstable portion of the cooling function, which was discussed in the previous section. The interstellar medium also contains star formation regions and molecular clouds, and the thick disk contains ionized warm gas.

The magnetic Reynolds number Rm from (1.2) and diffusion time τ_d from (1.3) can be roughly estimated for the interstellar medium. Assuming typical values of $\eta = 1/(\mu_o \sigma_o) \approx 10^{19}$ cm^2 s^{-1}, e.g., Korpi (1999), a scale height of ∼100pc, or about 3x10^{15} km, and a typical velocity of about 1 km/s, the resulting $Rm = 3 \times 10^6 \gg 1$, with the implication that the interstellar medium can be treated as ideal with minimal diffusion and the frozen-in condition from (1.4) applies. This also implies that the ISM is highly turbulent (e.g., Frisch 1995).

1.4 Galactic Magnetic Fields

The magnetic field is observed in two components, $\mathbf{B}_\perp$ and $B_\parallel$, where $\perp$ indicates observations of the field components perpendicular to the line of sight, and $\parallel$ is components parallel to the line of sight. $\mathbf{B}_\perp$ and the average $\langle \mathbf{B}_\perp \rangle$ are obtained from synchrotron emission. The challenge with measuring $\mathbf{B}_\perp$ lies in determining the contributions to measured synchrotron emission from sources unrelated to the magnetic field. This introduces a factor K, which is the ratio of the energy densities of cosmic rays to relativistic electrons, where the energy density of the cosmic rays is approximately the energy density of the magnetic field. Locally K $\simeq 100$, but it may be lower (Pohl 1993).

It is not entirely problematic, however, if one considers approaching the problem by taking filaments with a volume filling factor f so that the field strength of the equipartition estimate from K is smaller by a factor $f^{1/(3+\alpha_s)}$ where α_s is the synchrotron spectral index, $\simeq 0.9$. Significant error in K translates to a smaller error in field strength. The field strength measured is itself a lower limit.

$B_\parallel$ is obtained from Faraday rotation, the result of the birefringent properties of a magnetic plasma that affects left-hand and right-hand polarized light differently. Faraday rotation gives a rotation measure that is proportional to the average $B_\parallel$ and n_e, where n_e is the electron density. Typically this is given as an integral over the

distance from the observer to the object since neither n_e nor $B_\parallel$ is constant, so that

$$RM = C \int_0^d n_e B_\parallel dz, \tag{1.23}$$

where C is some constant. A simplified model has only three contributions to the observed polarization

$$\Psi = \Psi_o + RM\lambda^2 + RM_{fg}\lambda^2, \tag{1.24}$$

where Ψ_o is the polarization due to the transverse field, λ is the observed wavelength, RM is the rotation measure of the observed galaxy, and RM_{fg} is the rotation measure of the foreground. A minimum of observations at three different wavelengths is required to determine with some accuracy a rotation measure of a galaxy due to the foreground rotation, as well as its direction toward or away from the observer.

Observing $B_\parallel$ is not without some problems. Small HII regions within the thin disk and fluctuations within the warmer diffuse ionized gas in the thick disk are theorized to cause Faraday dispersion. Faraday depolarization occurs wherever an extended source exists, as even a strongly linearly polarized source will have different values for rotation measures due to the various emission locations.

The rotation angle Ψ is no longer proportional to λ^2 when observed at certain wavelengths. Full rotation measures are only possible in the Faraday-thin regime of $\lambda \leq 6$ cm, requiring observations at longer wavelengths to weigh regions on a basis of proximity to the observer.

1.4.1 Observational Evidence

Using these methods, many spiral galaxies have already been observed and their field strengths and configurations have been estimated. The results are all of similar magnitudes, with the resulting field strengths around $10 \pm 4\mu$G (Fitt & Alexander 1993). Certain galaxies have been measured to have fields as strong as 50 μG, and it should be noted that estimates are a lower limit as the capabilities of modern instruments are not enough to resolve stronger fields from the surrounding weaker areas.

Dozens of galaxies have been observed and magnetic fields mapped, with some particularly interesting results. Magnetic structure within a galaxy is classified by the symmetry of the azimuthal and vertical structures. In the azimuthal direction, axisymmetric structure is denoted ASS, while anti- or bi-symmetric structure is BSS.

Vertical Structure	Azimuthal Structure		
	ASS	BSS	MSS
Even	S0	S1	S0 + S1
Odd	A0	A1	A0 + A1
Mixed	Mo	M1	M0 + M1

Table 1.2: Labeling for magnetic structure based on vertical and azimuthal structure taken from Beck et al. (1996).

A combination of the two is denoted by MSS. If vertical structure is factored in, the notation is in Table (1.2). S stands for symmetric and A for antisymmetric, a dipole and a quadropole respectively.

The dominating candidate structure for most galaxies is ASS. Because of the position within the galaxy, the Milky Way's structure is difficult to observe, but it is generally assumed to be ASS. MSS galaxies are thought to be rarer, and BSS has only one candidate, M81 (Krause et al. 1989b). Gravitational interactions serve as a key characteristic of galaxies that are classified as MSS, which is a short list that includes M33, M81, and NGC 2276. BSS structure dominates in M81, while M33 and NGC 2276 are dominated by ASS structure.

M31 is an example of ASS, investigated by Beck (1982) and Ruzmaikin et al. (1990). It is unusual in that the structure appears to be an almost perfect torus. The toroidal field is measured to be $\simeq 7\mu$G, while the regular field strength is $\simeq 4\mu$G. There is some evidence of periodicity related to the $m = 1$ mode. Some theoretical contributing factors to the near-perfect structure of M31 are thought to be due to its low star formation rate and lack of grand-design spiral structure and therefore density waves to modify the field.

The only candidate for BSS, M81, has some interesting features studied by Krause et al. (1989b) and Sokoloff et al. (1992). The synchrotron emission from the galaxy is strongest along the optical arms, but the field is strongest in the less dense interarm space, parallel to the optical arms. This is counterintuitive to the frozen-in theory of MHD, where magnetic field lines frozen into the interstellar medium would be stronger and denser in areas where the gas is denser, suggesting that the magnetic field is not strongly coupled to all gas. The theory is further belied by the fact that magnetic

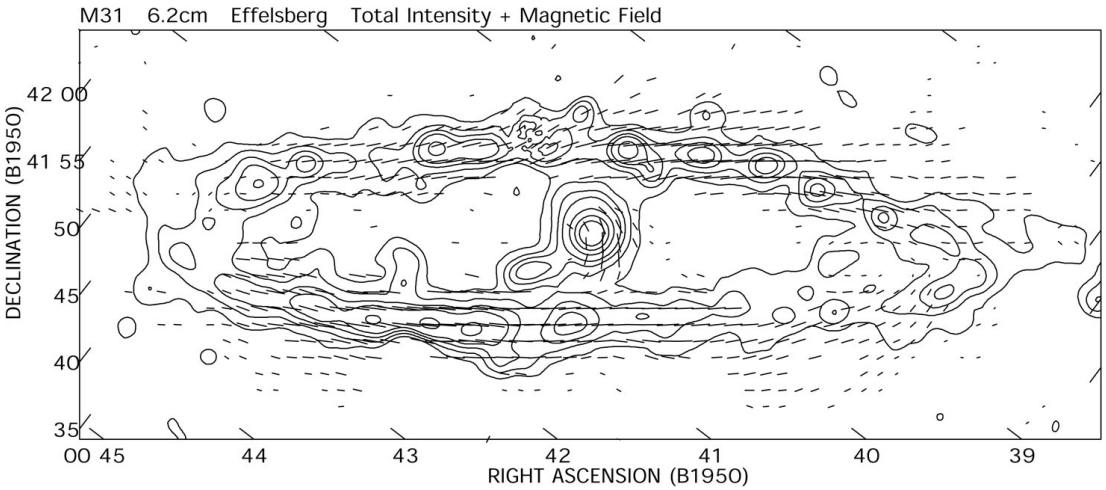

Figure 1.2: Magnetic Field of M31 - Shape and intensity of magnetic field of M31, taken at λ6.2cm Effelsberg 100m telescope, image taken from Berkhuijsen et al. (2003).

structure extends into areas where the optical data lack structure, implying that the magnetic field follows a structure that is not visible in the optical range.

Another well-studied galaxy is M51 (Horellou et al. 1992, Segalovitz et al. 1976), a candidate for MSS. Similarly to M31, it has a low star formation rate and much weaker spiral structure. Unlike M31, the magnetic field is not a torus but is instead visible as two strong spiral arms that lie approximately within the colder gas regions. There is no density wave compression of the magnetic field, but it appears that the field is coupled to regions of CO and HI gas, following the dust lane close enough to even cross the optical arm. This is confirmed by the observed polarization range of 10-30% being significantly less than the estimated value of polarization due to shock compression of 40-70% (Beck 1982).

Classification attempts are still approximate, and as higher resolution images become available more can be said about the overall structure. Observed structure must form from something, and there are several prevailing theories regarding the source of this magnetic field, mainly fossil theory and dynamo theory.

1.4.2 Fossil Theory

It has been known for over 40 years that the the Milky Way Galaxy possesses a magnetic field. Measurements from synchrotron emission, Faraday rotation, and Zeeman splitting

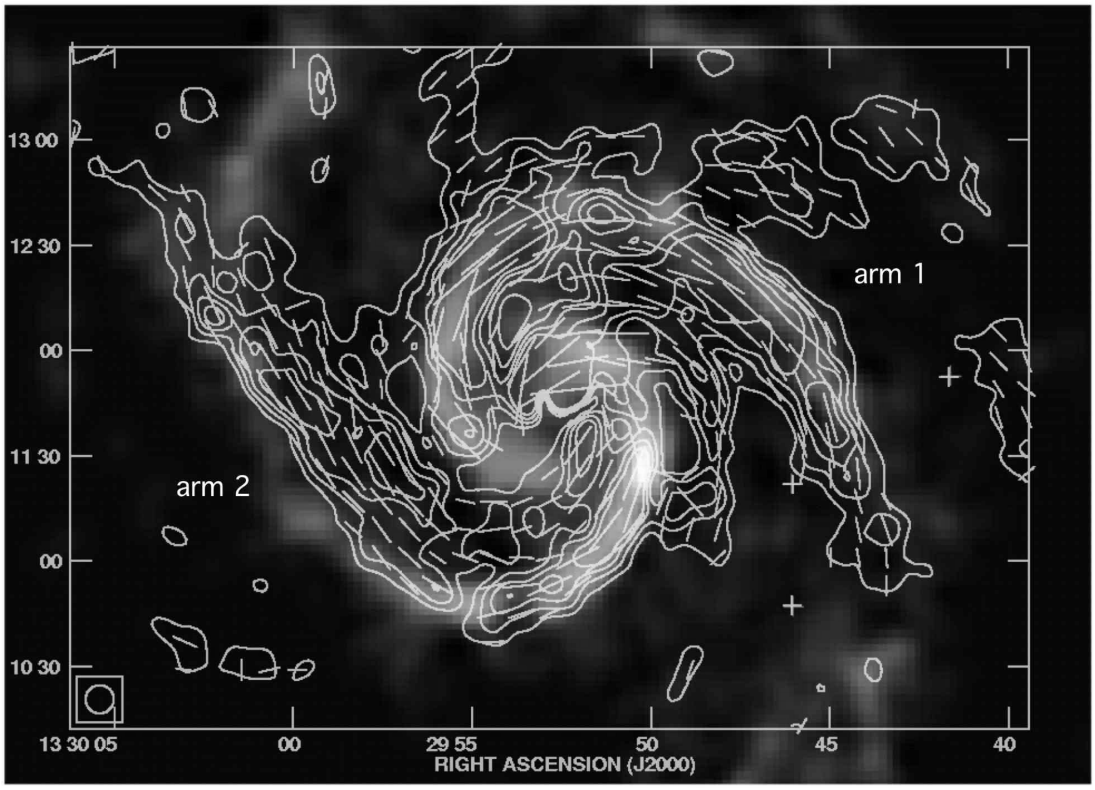

Figure 1.3: Magnetic Field of M51 - Contours of the λ6cm polarized radio emission (VLA and Effelsberg combined) of the center of M51 with Faraday-rotation corrected **B** overlaid on the map of integrated CO(10) line emission of Helfer et al. (2003).

have all confirmed the presence of magnetic fields in the Milky Way and other spiral galaxies. However, exact origins of the magnetic field are unknown, but one current prominent theory is that spiral galaxies can renew their magnetic fields through dynamo action, converting kinetic energy into magnetic fields.

The first explanations for a galactic-scale magnetic field began, however, with fossil theory. Some universal magnetic field, a seed field, would upon contraction grow in strength such that the magnetic field **B** was proportional to the density of an object to some power. Ruzmaikin, Shukurov, and Sokoloff (1988) demonstrated that a seed field of strength 10^{-10} G could easily create a compressed field of 10^{-7} G for a protogalactic collapsing cloud. A collapsing magnetic field strength can be approximated so that the magnetic field strength is directly proportional to the inverse squared of the radius of a collapsing cloud.

Such a cloud lacked the observed axisymmetric structure of the magnetic field observed in most spiral galaxies, however. It is also problematic in that studies by Enqvist et al. (1993, 1995) and Mishustin and Ruzmaikin (1971), among others, placed limitations on a universe-wide homogeneous relic magnetic field of around 10^{-20} G, which is many orders of magnitude less than what is needed for the collapse process described above to work.

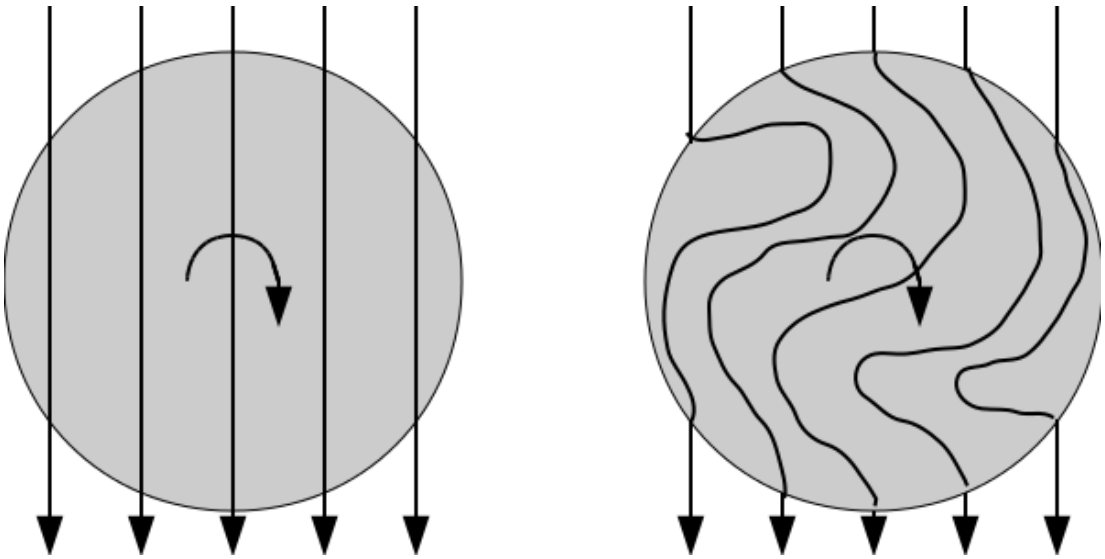

Figure 1.4: Winding of Magnetic Field - Any frozen field that experiences winding will have the field altered. With each twist, the field lines come closer together, making reconnection likely.

Galaxies are known to rotate differentially, i.e., the outer parts rotate more slowly than the inner parts, forming the spiral shapes. If a frozen-in magnetic field was to be subject to such winding, it would be forced to follow the spiral shape of the gas. Evidently, the field would be amplified during such a process. But any such winding would not sustain a field, as it can be seen from the diagram that as a field is wound up, it will lose structure as the field lines become closer together, until eventually all spiral structure is lost. It can be seen that even a partial turn complicates the field far beyond the simple spiral structure observed in most magnetic fields in spiral galaxies today. A magnetic field that shows the strength and stucture observed in present times in spiral galaxies must have a a more complex means of being generated than fossil field theory.

1.4.3 Dynamo Theory

The application of dynamo theory helps to solve some of these problems facing the origin and structure of such strong magnetic fields present in spiral galaxies. The theory is that galactic turbulence could maintain the large-scale field in a galaxy. Because of the quadrupole nature of most observed galaxies, the dynamo model most often applied is the $\alpha^2\omega$ dynamo, based on helical turbulence and differential rotation.

The shape of the galaxy is usually taken to be a thin disk embedded in a spherical shell to represent the disk and halo. The disk is stratified, and observed quantities give a scale height $h \sim 0.5 - 1$ pc. Typical values for the rotation Ω are of the order 20 km/s/kpc and root mean square turbulent velocities v of 10 km/s.

The basic dynamo equation is obtained with mean field theory. The velocity and magnetic field take the form of some average (denoted by $\langle\ \rangle$) added with small fluctuations

$$\mathbf{B} = \langle \mathbf{B} \rangle + \mathbf{b} \tag{1.25}$$

and

$$\mathbf{U} = \langle \mathbf{U} \rangle + \mathbf{u}, \tag{1.26}$$

where $\langle \mathbf{b} \rangle = \langle \mathbf{u} \rangle = 0$. Substituting these into the induction equation (1.1) yields

$$\frac{\partial \langle \mathbf{B} \rangle}{\partial t} = \nabla \times (\langle \mathbf{U} \rangle \times \langle \mathbf{B} \rangle + \boldsymbol{\mathcal{E}} - \eta \times \langle \mathbf{B} \rangle) \tag{1.27}$$

and

$$\frac{\partial \mathbf{b}}{\partial t} = \nabla \times (\langle \mathbf{U} \rangle \times \mathbf{b} + \mathbf{u} \times \langle \mathbf{B} \rangle + G - \eta \nabla \times \mathbf{b}), \tag{1.28}$$

for the mean and fluctuating parts, respectively. The mean turbulent electromotive force $\boldsymbol{\mathcal{E}}$ is

$$\boldsymbol{\mathcal{E}} \equiv \langle \mathbf{u} \times \mathbf{b} \rangle, \tag{1.29}$$

and

$$G = \mathbf{u} \times \mathbf{b} - \boldsymbol{\mathcal{E}}. \tag{1.30}$$

If the field is not too intermittent, it can be expanded into the form (e.g., Krause & Rädler 1980),

$$\varepsilon_i = \alpha_{ij} \langle B_j \rangle + \frac{\eta_{ijk} \partial \langle B_k \rangle}{\partial x_k} + ... \tag{1.31}$$

where α_{ij} and η_{ijk} are anisotropic tensors depending on shear, stratification, rotation, and the general magnetic field. Under first-order smoothing approzimation (FOSA), only the two leading terms in the expansion are kept. Turbulence leads both to an inductive effect and enhanced diffusion. With the help of this approximation, Rüdiger and Kitchatinov (1993) gave more explicit solutions.

The α-tensor and η can be approximated as

$$\alpha \approx -\ell^2 \Omega \cdot \nabla \ln(\rho v) F(\langle \mathbf{B} \rangle, \Omega) \tag{1.32}$$

and

$$\eta_t \approx \frac{1}{3} v \ell G(\langle \mathbf{B} \rangle, \Omega), \tag{1.33}$$

where ℓ is the correlation length, α and η_t have been reduced to scalars from full tensor quantities, and F and G are quenching functions. The mean part (1.28) is of interest when discussing the global galactic magnetic field evolution. Both helical turbulence, described by the α-term (also known as the $\alpha - effect$), and the magnetic diffusivity η are important, and the mean-field dynamo equation for thin disks takes the form, using (1.27) and (1.28),

$$\frac{\partial \langle \mathbf{B} \rangle}{\partial t} = \nabla \times (R_\omega \times \langle \mathbf{B} \rangle + R_\alpha F \langle \mathbf{B} \rangle - G \eta_t \nabla \times \langle \mathbf{B} \rangle), \tag{1.34}$$

where $R_\omega = h^2 \Omega / \eta_t$ is a dimensionless shearing number based on the characteristic time scale and rotation, and $R_\alpha = h\alpha / \eta_t$ is a dimensionless number characterizing the alpha effect based on the scale height and the magnitude of the α-effect. $F(\langle \mathbf{B} \rangle, \Omega) =$

$(1 + \langle \mathbf{B} \rangle^2 / B_{eq}^2)^{-1}$ is a form of α quenching and $G(\langle \mathbf{B} \rangle, \Omega)$ is the quenching function for turbulent diffusivity. Because G is largely unknown, it is common practice to set it equal to unity. The form is useful in that the exponentially growing solutions needed to maintain a dynamo can can be characterized by the dimensionless number $D = R_\alpha R_\omega \approx 10$, above which a dynamo can operate. For rough estimates, this is simplified to

$$D \simeq 9(\frac{h\Omega}{v})^2. \tag{1.35}$$

Thus it can be shown that for typical galaxies, D $\sim$ 10 and the $\alpha^2\omega$ dynamo can be expected to operate.

The exact mechanisms for maintaining the dynamo are not as clearly defined. The turbulence can have a variety of sources. This thesis explores the effect of thermal instability in the gas, but there are other possible contributing factors to turbulence. Supernovae alone are powerful enough and frequent enough to expel energy and create turbulence to maintain a dynamo, averaging 1 every 50 years in one galaxy at an average strength of 10^{51} ergs. It is clear, however, that the mechanism for a galactic dynamo must be different from the dynamo that operates in the sun, for instance. The solar magnetic field reverses direction every 11 years or so, implying a dynamo that operates with a much smaller time scale than the billions of years in galaxies.

2

Method

The aim of this thesis is to explore the effects that the thermal instability (hereafter TI) has on the formation and efficiency of a dynamo in the interstellar medium. For this purpose, the gas to be numerically simulated was isolated from normal galactic effects, such as supernovae, that are possible contributors to dynamo action as well as a source of hot ionized gas. The effect TI has on a dynamo is unknown, though there is a certain amount of mixing and turbulence that TI naturally creates as it separates matter into warm and cold phases. It might be possible for such an effect to make a dynamo formed in gas with an unstable cooling function more efficient. Turbulence and a seed field must be introduced into the system in order to grow a dynamo with a large-scale field.

Two possible types of dynamos can arise: the large-scale and the small-scale. The existence of both is supported by observational evidence. However, the contributing factors to both scales are not entirely known. Brandenburg (2001) investigated numerically simulated isotropic helically forced fields. It was found that net kinetic helicity produces a force-free magnetic field provided the simulation is at or above the critical Rm, from equation (1.2). The resulting field depends on the shape of the computational domain, and, in the cases of periodic boxes, the field resembles a sinusoidal Beltrami field, slightly distorted by turbulence. If no such net helicity exists, then there is no large-scale field. If the critical Rm is reached for both the small-scale and large-scale fields, both may be present. Typically the Rm for the large-scale field is a magnitude smaller than the Rm for the small-scale field.

Turbulence suppresses the magnetic energy at smaller scales so that energy input is from the small-scale to the large-scale. This is suggestive of an α^2, as opposed to the α-ω that operates at lower Rm with the presence of shear. This is for the case of helical forcing only; other factors such as shear or magnetorotational instability may contribute to creation of large-scale and small-scale dynamos but are not included in this project.

The effects of nonhelical forcing are further explored to examine another component of the magnetic field, the small-scale field. The critical Rm required to form a small-scale dynamo in nonhelical isothermal flows was explored by Haugen et al. (2004). The result is that a high Rm is required for dynamo action. In the subsonic regime, $Rm > 30$ was required and in the supersonic regime, $Rm > 70$ was required for dynamo action. As the Mach number approaches 1, the critical Reynolds number is ~ 60.

The Pencil Code uses artificial diffusion to handle discontinuities such as shocks, but because its effects on TI properties are unknown, it is more desirable to restrict simulations to $Ma < 1$. Numerical simulations must have a forcing value strong enough to create a small-scale dynamo but weak enough for the gas to remain subsonic. An attempt will be made to explore the limit of forcing by increasing the forcing while keeping the Mach number under 1 to avoid crashing the code. In theory, a run with nonhelical forcing and Rm above the critical value for the dynamo should create the small-scale dynamo.

2.1 The Pencil Code

The Pencil Code began development at the Turbulence Summer School of Helmholtz Institute in Potsdam in 2001 and is continuously updated and customized for research. It uses high-order first- and second-order derivatives to model weakly compressible turbulent flows using explicit finite differences. It is nonconservative, but as it was created primarily to deal with magnetic fields, dynamos, and magnetic helicity the absolute conservation of quantities is only required to the level of the problem and not to machine precision. It is sixth-order in space and third-order in time. More information about the Pencil Code and the code itself are available at http://www.nordita.org/software/pencil-code/.

The code uses the standard compressible MHD equations including the continuity equation (1.12), the equation of motion (1.13), and the entropy equation (1.14), and the equation for magnetic vector potential is

$$\frac{\partial \mathbf{A}}{\partial t} = \boldsymbol{u} \times \mathbf{B} - \eta \mu_o \boldsymbol{J}, \tag{2.1}$$

where $\mathbf{B} = \nabla \times \mathbf{A}$ is the magnetic field, $\eta = 1/(\mu_o \sigma)$ is the magnetic difusivity, and $\mathbf{J} = \mu_o \nabla \times \mathbf{B}$ is the current. The vector potential is used in place of directly calculating the magnetic field to guarantee that $\nabla \cdot \mathbf{B} = 0$ at all times.

The net heating is $\mathcal{L}$ and of the form from (1.17), $\mathcal{L} = \rho\Lambda - \Gamma$. Γ is assumed to be a constant of approximately 0.015 ergs g^{-1} s^{-1} at $n = 1$ cm^{-3}, the photoelectric heating by interstellar grains as determined by Wolfire et al. (1995). Λ is the cooling function and is fitted to a piece-wise power law (1.18) that can be either stable or unstable in individual sections based on the isobaric instability criteria (1.21), as detailed in Section 1.2.2.

Hydrodynamical (HD) simulations do not solve for the magnetic field; therefore, (2.1) is not used for HD runs, and the flow is considered purely hydrodynamical. Such simulations were used to analyze the effects the helical forcing has on the velocities in the absence of a magnetic field for comparison.

Diffusive effects, particularly thermal diffusion, can stabilize TI, as is demonstrated in the following analysis, as first presented by Field (1965). Here, the treatment and notations as presented in Brandenburg, Korpi, and Mee (2007) are used.

Assuming solutions proportional to $\exp(nt + i\mathbf{k} \cdot \mathbf{x})$ and including the effects of thermal and kinematic viscosity yields a dispersion relation as follows:

$$n(n + n_\nu)(n + \beta n_\rho + n_\chi) + \omega_{ac}^2 \left[n + \frac{(\beta - 1)n\rho + n\chi}{\gamma} \right] = 0, \tag{2.2}$$

where $\omega_{ac}^2 = c_s k$ is the acoustic frequency and β is local value from equation (1.19). The net heating is from equation (1.17) with Γ held at some constant and Λ is a function of only T. The cooling rate then becomes

$$n_\rho = \frac{\rho_o \mathcal{L}_\rho}{c_v T}, \tag{2.3}$$

where n_ρ is similar to the form given by Field (1965), who used $k_\rho = n_\rho / c_s$. The viscous and diffusive effects are characterized by the corresponding rates $n_\nu = \frac{4}{3}\nu k$ and $n_\chi = \gamma \chi k^2$, respectively.

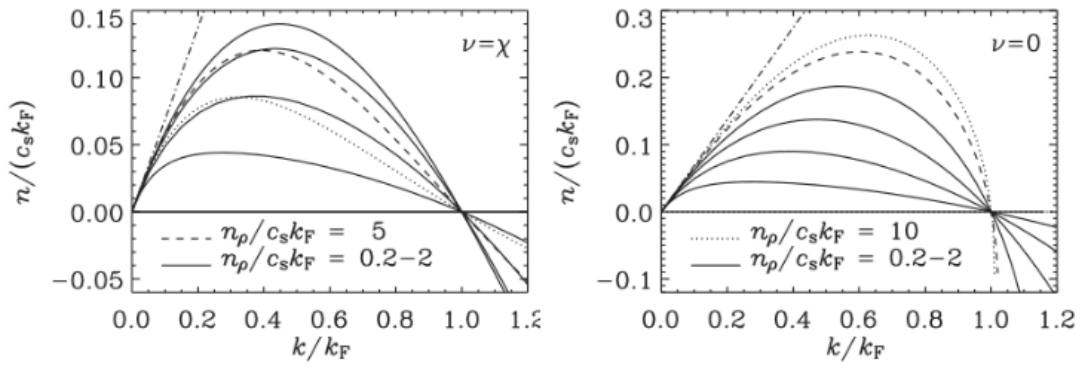

Figure 2.1: Dispersion Relation - Growth rate $n(k)$ for $\beta = 0.56$. Curves are normalized in terms of k_F and $c_s k_F$. The diagonal dot-dash line is an approximation valid for small wavenumbers. Brandenburg, Korpi, and Mee (2007).

If k_1 denotes the largest wavenumber (and Δx is the corresponding smallest length scale) of the system, then to stabilize the gas $k_1 > k_F$, where k_F is now the Field length defined to be

$$k_F^2 = \frac{(1-\beta)n_\rho}{\gamma\chi}, \tag{2.4}$$

and the criterion becomes

$$\chi > \frac{(1-\beta)n_\rho}{\gamma\Delta x^2}. \tag{2.5}$$

This property of TI can be used to keep the Field length on the grid so that $\Delta x, \Delta y, \Delta z > k_F$ at all times using this criterion. In addition to Brandenburg, Korpi, and Mee (2007), this approach is also used by Koyama and Inutsuka (2004), who found the optimal grid size to be approximately three cell lengths per Field length for numerical simulations to converge. This is illustrated in Figure 2.1, where kinetic viscosity and thermal diffusivity have equal strength ($\nu = \chi$). χ stabilizes the Field length to keep it on the grid, so that numerical simulations can converge. From this figure it can be seen that the normalized growth rate decreases when diffusive effects are added.

2.2 Project

The goal of the thesis is to investigate the effect of TI on the creation and efficiency of different types of dynamos using standard values for the interstellar medium, external forcing, and a small random seed field for magnetohydrodynamical cases.

The efficiency of the dynamos can be determined by examining the resulting growth and saturation value of the magnetic energy. In theory, a flow with a higher level of turbulence (and as a result, kinetic energy) would create the dynamo more efficiently. TI creates some level of turbulence as the gas is continuously pushed out of the stable states into the unstable regime before moving back to a stable state. This additional turbulence from TI could create a more efficient dynamo than a stable cooling function.

Thermal energy (or internal energy), kinetic energy, and magnetic energy are all computed directly from the simulation using the following equations:

$$E_{therm} = \int_V \rho e dV, \tag{2.6}$$

$$E_{kin} = \int_V \frac{1}{2}\rho u^2 dV, \tag{2.7}$$

and

$$E_{mag} = \int_V \frac{1}{2\mu_o} B^2 dV, \tag{2.8}$$

respectively, where $e = c_v T$ is the internal energy, and $\int_V$ for all is integrated over the total volume of the computational domain.

In theory, the dynamo growth is expected to saturate when the magnetic field energy approaches the kinetic energy of the turbulence, or equipartition. The magnetic field starts to quench its own generators by affecting the velocity field. The more supercritical the dynamo is, i.e., the larger its forcing amplitude, the more quickly the dynamo is expected to reach the saturated state. In the project setups, however, the growing magnetic field cannot influence the forcing amplitude, although the field is capable of affecting the turbulent velocity field. Therefore, the system cannot be expected to behave in a completely natural way, but at least in the linear regime where the magnetic field is still weak, the results such as the growth rate and critical Rm should not be affected.

The nonlinear saturation of dynamos has been under considerable debate during recent years. The current consensus (see, e.g., Brandenburg and Subramanian, 2005) is that dynamos are able to saturate at high Rm, in realistic time scales and reaching realistic amplitudes, only if the dynamo is capable of getting rid of small-scale magnetic helicity. In closed domains, such as the periodic box considered in this study, no helicity fluxes out of the domain can occur. Therefore, the dynamo can be expected to saturate very slowly, on a sensitive time scale.

2.2.1 Parameters and Setups

The purpose of the setups was to numerically simulate differences between thermally stable and unstable gas. The properties of the simulated ISM are made to resemble common interstellar matter in spiral galaxies, and the size of the computational domain is chosen to match the one at which the large-scale dynamo action is believed to occur in spiral galaxies.

Unit	Value
$[\ell]$	3.1557 x 10^{21} cm $\sim$ 1 kpc
$[u]$	1 km s^{-1}
$[\rho]$	1 x 10^{-24} g cm^{-3}
$[B]$	0.354491 μG
$[T]$	1 K
$[p]$	10^{-14} dyn
$[t]$	1 Gyr
$[E]$	3.14259 x 10^{50} ergs

Table 2.1: Units - units for numerical setups

The unit of time is chosen to be 1 Gyr. The ages of spiral galaxies are estimated to be a magnitude higher than this. A successful dynamo would have to saturate within this time scale in order to correspond to the current observed magnetic fields in spiral galaxies. $[u]$ is the order of typical velocity dispersion in the ISM of both warm and cold phases. From these two quantities, the length scale $[\ell]$ is set and happens to be of the order of 1 kpc.

The size of the numerical simulation was cubic box of proportions $(0.2[\ell])$ with periodic boundary conditions. The correlation length of interstellar turbulence, ℓ_o, is of the order of 50 – 100 pc calculated by Korpi et al. (1999), and so the simulation is approximately $(2\ell_o)^3$ and contains several full turbulent cells. Brandenburg, Korpi, and Mee (2007) estimated the minimum cell size required to resolve TI (and the Field length) to be around 24 pc for values of $\chi = 0.005$ Gyr km^2 s^{-2} and the Prandtl number fixed to unity. The simulation is sufficiently large to resolve the TI with a resolution of 128^3.

The density is based on the standard estimated interstellar average density of 1 particle per cubic centimeter in the solar neighborhood. The simulation is designed to

resemble such a region in a typical spiral galaxy near the mid-plane. This is further adjusted in the setups by assuming an average mass for each particle of about 1.67 $\times 10^{-24}$ g cm^{-3}, or the mass of a proton. Small density fluctuations with a Gaussian distribution with the amplitude $\pm\ 10^{-2}\,[B]$ are used to seed TI. The temperature range of the ISM is about 50 – 10^4K from the cold, denser parts to the warm, diffuse gas, not including the more extreme temperatures caused by supernova explosions. The temperature is initially uniform and calculated from the isobaric condition.

The region simulated is purposely chosen to be near the mid-plane of the galaxy to avoid stratification, and in a quiescent region. This is physically realistic as most supernova explosions are located at OB associations, leaving regions where other factors, including thermal instabilities, may be more important. However, supernova explosions are considered to be a major factor in creating the helical forcing that creates the large-scale dynamo, and therefore the scale at which dynamo action occurs must correlate with the scale of turbulence created by supernovae.

As discussed in section (1.4), magnetic fields of galaxies are typically in the 10 ± 4 μG range for a saturated large-scale magnetic field. Thus, the observed dynamo-saturated field should have a strength of this order with reasonable forcing in order to determine the effects of TI.

In addition to the density being set to the mass of a proton per cm^3, other parameters were set to be constant. In order to obtain an instability in isobaric conditions ($\beta < 1$ from (1.21)), the pressure was initially set to 55.1975 x 10^{-14} dyn, which provided temperatures within the range of the ISM but steadied on a constant value more appropriate for the average temperature and density of the simulation as it cooled. Entropy was set to keep this value constant.

The cooling function used the constants in Table (2.2) depending on whether the setup is unstable or stable. The heating Γ from (1.17) was set to be a constant of the value of 0.015. The magnetic field was seeded by random perturbations with a Gaussian distribution of a maximum deviation ± 0.001 for those runs that included a magnetic field. During the run, magnetic diffusivity η was set to be a constant value of 0.005 Gyr km^2 s^{-2}. Kinetic viscosity ν was a constant value of 0.005 Gyr km^2 s^{-2}. Thermal diffusivity χ was also a constant 0.005 Gyr km^2 s^{-2}, a magnitude above the required minimum value needed to keep the Field length on the grid. This satisfied the

condition that both the Prandtl number and the magnetic Prandtl number be unity, i.e., $Pr = \nu/\chi \equiv 1$ and $Pr_m = \nu/\eta \equiv 1$.

Turbulence was introduced via external forcing. The amplitude varied and the helicity was ± 1 for all simulations except those with nonhelical forcing, which instead used a value of exactly 0. External forcing is added to equation of motion (1.13) as follows:

$$\rho \frac{D\mathbf{u}}{Dt} = -\nabla p + \nabla \cdot (2\nu\rho\mathbf{S}) + f, \tag{2.9}$$

where f is the external forcing. For the project, the forcing was artificial. In the case of the true ISM, forcing can result from shear, magnetorotational instabilities, and supernovae. Forcing in the Pencil Code is calculated as

$$f(\mathbf{x}, t) = Re\{\mathrm{N} f_{\mathbf{k}(t)} \exp\left[i\mathbf{k}(t) + i\phi(t)\right]\}. \tag{2.10}$$

$\mathrm{N} = f_o c_s \left(k c_s/\delta t\right)^{1/2}$ is the normalization factor where f_o is a non-dimensional forcing amplitude, δt is the time step of the simulation, and $k = |\mathbf{k}|$.

The purpose of the hydrodynamical simulations was to trace the properties of the gas itself when not subjected to a magnetic field. These setups were identical in all aspects to their magnetohydrodynamical counterparts except for the inclusion of magnetic effects. The purpose of such setups is to compare the resulting velocities, pressures, energies, and densities to determine the effect of the unstable and stable cooling functions on the properties of the gas itself in the absence of a magnetic field.

2.2.2 The Cooling Function

The cooling function is the cooling portion of (1.17). It is a piecewise power law (1.18) that can be put in the following form where i,$i+1$ indicates the interval over which the constants are valid:

$$\Lambda_i = C_{i,i+1} T_i^{\beta_{i,i+1}}, \tag{2.11}$$

where C and β are constants determined by the type of cooling function. Table (2.2) contains the values that were used for the unstable and stable runs.

Two different cooling functions were selected for comparison, one stable and one unstable. The unstable curve was based on the function determined by Sanchez-Salcedo et al. (2002). This unstable curve was determined by fitting the power law to observations by Wolfire et at. (1995) with some adjustment to ensure a continuous function.

Table 2.2: Coefficients for the thermally unstable (U) and stable (S) cooling curves.

i	T_i	$C^U_{i,i+1}$	$\beta^U_{i,i+1}$	$C^S_{i,i+1}$	$\beta^S_{i,i+1}$
1	10	3.42×10^{16}	2.12	2.16×10^{17}	1.50
2	141	9.10×10^{18}	1.00	2.56×10^{18}	1.00
3	313	1.11×10^{20}	0.56	2.56×10^{18}	1.00
4	6102	2.00×10^{8}	3.67	2.00×10^{8}	3.67
5	10^5	7.96×10^{29}	-0.65	7.96×10^{29}	-0.65

The stable curve was based on a fit to the the unstable cooling function with a stable portion inserted ($\beta = 1$) where previously the function was unstable ($\beta > 1$). The lower end of the cooling function was then adjusted to prevent spiking and to maintain equal energy at constant density, so that the integrals of the two cooling functions were equal. Previously published cooling functions, such as the stable cooling function created by Rosen and Bregman (1993), varied slightly in the desired range as to this total energy and were not suitable for this sort of comparison. The stable cooling function used for this project was completely artificial and made specifically for this project. The purpose was to study the role of TI on the dynamo, and it was important to keep $\mathcal{L}$ =const for both functions to create a legitimate comparison.

The stable curve was minimally altered with very few differences between the stable and unstable functions for the average temperatures of the simulations. Values for the purposes of creating a function of equal energy to the SS cooling function were computed by integrating the entire cooling function over the temperature range of 10K to 10^5K for a constant density. Higher temperatures were not considered for the purpose of this thesis because of the nature of the gas simulated in this project. In principle, the helical forcing created by supernovae could easily create temperatures that exceed 10^5 K. The earlier runs for the project were checked to verify that the maximum temperatures of all runs would be well within this temperature limit.

2.3 Summary of Runs

For simplification purposes, the various runs will be referred to in the following shorthand in Table (2.3) that contains all the information regarding the parameters for each

run. Runs will be referred to by this labeling system for ease of reference. Additionally, runs indicated in bold are the runs for this specific thesis while the rest of the runs were made to complete the resulting publication by Mantere et al. (2011). These additional runs are used to provide a more complete picture of the results.

RunID	**Cooling Function**	**Magnetic**	**Forcing**	**Helicity**
sHD30	S	HD	15	1
HDTSa	S	HD	20	1
sHD15	S	HD	30	1
HDTSb	S	HD	50	1
sHD30	S	HD	60	1
HDTSc	S	HD	70	1
uMHD15	U	HD	15	1
HDSSa	U	HD	20	1
uMHD30	U	HD	30	1
HDSSb	U	HD	50	1
uMHD60	U	HD	60	1
HDSSc	U	HD	70	1

Table 2.3: Run Parameters for Project - parameters for runs based on reference ID. Runs for this thesis are indicated in bold. U stands for the unstable cooling function while S indicates a stable cooling function.

RunID	Cooling Function	Magnetic	Forcing	Helicity
TSf	S	MHD	7	1
TSe	S	MHD	10	1
sMHD15	S	MHD	15	1
TSa	S	MHD	20	1
sMHD30	S	MHD	30	1
TSd	S	MHD	35	1
TSb	S	MHD	50	1
sMHD60	S	MHD	60	1
TSc	S	MHD	70	1
SSe	U	MHD	10	1
SSf	U	MHD	15	1
uMHD15	U	MHD	15	1
SSa	U	MHD	20	1
uMHD30	U	MHD	30	1
SSd	U	MHD	35	1
SSb	U	MHD	50	1
uMHD60	U	MHD	60	1
SSc	U	MHD	70	1
TSanh	S	MHD	20	0
TSbnh	S	MHD	50	0
TScnh	S	MHD	70	0
SSanh	U	MHD	20	0
SSbnh	U	MHD	50	0
SScnh	U	MHD	70	0
uMHDnh90	U	MHD	90*	0
uMHDnh140	U	MHD	140*	0

Table 2.4: Run Parameters for Project - parameters for runs based on reference ID. $*$ indicates a final forcing value. Runs for this thesis are indicated in bold. U stands for the unstable cooling function while S indicates a stable cooling function.

3

Results

The models were run on the Murska cluster at the CSC IT Center for Science Ltd. in Espoo, Finland. The CSC is a non-profit company that provides IT support and resources for academia, research institutes, and companies. Murska is an HP CP4000 BL ProLiant supercluster. It has 2176 compute cores. More information about the CSC can be found at http://www.csc.fi/.

The simulations for this thesis were run with 16 cores and each individual model consumed over 800 CPU hours. This thesis is part of a larger project totalling over 52,000 CPU hours, part of the quota for the project "MHD-turbulence, dynamos, stellar surface mapping" at the CSC. The Pencil Code has been parallelized with the Message Passing Interface (MPI). The data was processed using IDL (Interactive Data Language), and the Pencil Code provides many useful custom routines for analyzing data outputted by the code.

All MHD models for this thesis were run to a minimum of 10 Gyrs except for those that used nonhelical forcing. The special case for nonhelical models is discussed later in this section. In all cases, 10 Gyrs was more than sufficient to determine the presence of a dynamo and for values to saturate and become approximately constant. Table (3.1) contains the summary of results of models run specifically for this thesis. HD models were run until values remained approximately constant.

Model	Forcing	$u_{\rm rms}$ [kms^{-1}]	$E_{\rm th}$	$E_{\rm kin}$	Ma$_{\rm rms}$	Rm
TSf*	7	0.891	–	0.005	–	–
TSe*	10	1.210	–	0.010	–	–
SSf*	15	3.400	–	0.034	–	–
sHD15	15	1.876	0.945	0.023	0.209	25
uHD15	15	2.401	0.394	0.036	0.423	32
HDTSa	20	2.453	0.945	0.038	0.271	33
HDSSa	20	3.299	0.433	0.042	0.434	44
sHD30	30	3.783	0.946	0.088	0.416	50
uHD30	30	4.562	0.494	0.033	0.351	61
SSd*	35	4.560	–	0.046	–	–
TSd*	35	3.650	–	0.086	–	–
HDSSb	50	6.023	0.564	0.082	0.528	80
HDTSb	50	5.648	0.945	0.186	0.617	75
sHD60	60	6.580	0.944	0.245	0.716	88
uHD60	60	7.01	0.604	0.093	0.093	93
HDTSc	70	7.762	0.943	0.342	0.848	103
HDSSc	70	8.114	0.630	0.145	0.679	108

Table 3.1: Summary of HD results from entire project. Runs specifically for this thesis are indicated in bold. Remaining runs are from Mantere et al. (2011). Units, unless otherwise indicated, are from Table (2.1). Runs marked with $*$ are values taken from MHD runs before the magnetic field has formed.

Model	Forcing	$\frac{u_{\rm rms}}{u_{\rm rms}^{\rm HD}}$	$\frac{b_{\rm rms}}{B_{\rm eq}^{\rm HD}}$	$E_{\rm th}$	$E_{\rm kin}$	$E_{\rm mag}$	$\mathrm{Ma}_{\rm rms}$	Rm	$\lambda_{\rm B}$ [Myrs]
TSf	7	1.000	–	0.943	0.005	–	0.100	12	–
TSe	10	1.000	0.461	0.944	0.010	0.002	0.135	16	500
SSe g	10	2.118	–	0.387	0.018	–	0.300	28	–
SSf	15	1.000	0.204	0.428	0.034	0.002	0.392	45	510
sMHD15	15	0.852	0.861	0.945	0.017	0.014	0.179	21	151
uMHD15	15	0.772	0.248	0.429	0.005	0.003	0.138	25	510
TSa	20	0.837	0.964	0.946	0.028	0.028	0.230	27	89
TSanh	20	0.960	–	0.946	0.036	–	0.264	31	–
SSa	20	0.930	0.436	0.447	0.021	0.007	0.289	52	200
SSanh	20	0.882	–	0.436	0.029	–	0.351	39	–
sMHD30	30	0.755	0.924	0.948	0.054	0.062	0.320	38	61
uMHD30	30	0.639	0.973	0.483	0.013	0.017	0.221	39	94
SSd	35	0.953	0.732	0.494	0.023	0.022	0.282	58	69
TSd	35	0.927	1.020	0.948	0.074	0.064	0.377	49	45
SSb	50	0.767	0.829	0.558	0.043	0.048	0.371	62	55
SSbnh	50	0.908	–	0.552	0.067	–	0.467	73	–
TSb	50	0.847	0.949	0.952	0.147	0.137	0.527	64	37
TSbnh	50	0.910	–	0.951	0.171	–	0.571	69	–
sMHD60	60	0.845	0.929	0.955	0.187	0.174	0.596	72	32
uMHD60	60	0.839	0.985	0.599	0.070	0.074	0.460	73	40
TSc	70	0.860	0.837	0.958	0.263	0.203	0.703	89	27
TScnh	70	0.878	–	0.954	0.294	–	0.750	91	–
SSc	70	0.676	0.873	0.628	0.067	0.094	0.422	73	33
SScnh	70	0.985	–	0.634	0.117	–	0.583	97	–
uMHDnh90	90	1.000	–	0.712	0.182	–	0.694	110	–
uMHDnh140	140	1.000	–	0.746	0.182	–	0.950	151	–

Table 3.2: Summary of results from all MHD runs for project. Runs in bold were done specifically for this thesis and all runs are part of a project for Mantere et al. (2011). Units unless otherwise indicated are from Table (2.1).

3.1 Hydrodynamical Simulations

The purpose of the HD runs was to determine the effects of the TI isolated from magnetic effects. Important values from the HD runs are listed in Table (3.1). The root-mean-square value (hereafter rms) for velocity, $u_{\rm rms}^{HD}$ is used to calculate a normalization factor $B_{\rm eq}^{HD}$ for the MHD simulations in Table (3.2) with the corresponding equipartition magnetic field strength calculated by using $B_{\rm eq}^{HD} = \sqrt{8\pi} E_{\rm kin}^{\rm HD}$. The normalization isolates the effect of the magnetic field on the flow.

Density and entropy are directly numerically solved for. The temperature and pressures can be calculated based on the outputted density and entropy using standard thermodynamics for an ideal monatomic gas:

$$\ln\left(\frac{T}{T_o}\right) = \frac{\gamma}{c_p} s + \frac{\gamma - 1}{\gamma} \ln\left(\frac{\rho}{\rho_o}\right), \tag{3.1}$$

$$c_v = \gamma c_p, \tag{3.2}$$

and

$$p = (\gamma - 1)\, c_v T \rho, \tag{3.3}$$

where T is the temperature, p is pressure, s is the entropy, c_p is the specific heat, and $\gamma = \frac{5}{3}$ for an ideal gas. By isolating a particular time slice, a probability density function (hereafter PDF) was created for the thermodynamic quantities that demonstrates visually the state of the gas.

The stable cooling function can only create a single peak as the gas stabilizes around one single value. The effect of stronger forcing is to increase mixing which results in a wider range of values for density, pressure, and temperature, as demonstrated by the wider peaks in Figure (3.1). In addition to more extreme values, stronger forcing also results in an increased average temperature and decreased density.

The unstable cooling function creates entirely different distribution functions. TI segregates the gas into two distinct states as demonstrated by the bimodal distributions for the PDFs in Figure (3.1). As discussed earlier in Section 2.2, there is a regime of temperatures where the gas is unstable. TI takes place under isobaric conditions and there are matching regimes for density and pressure. From the PDFs it can be seen that the two phases are not discrete and that gas can exist in this "forbidden" regime, indicating the added turbulence created by gas being continually pushed into

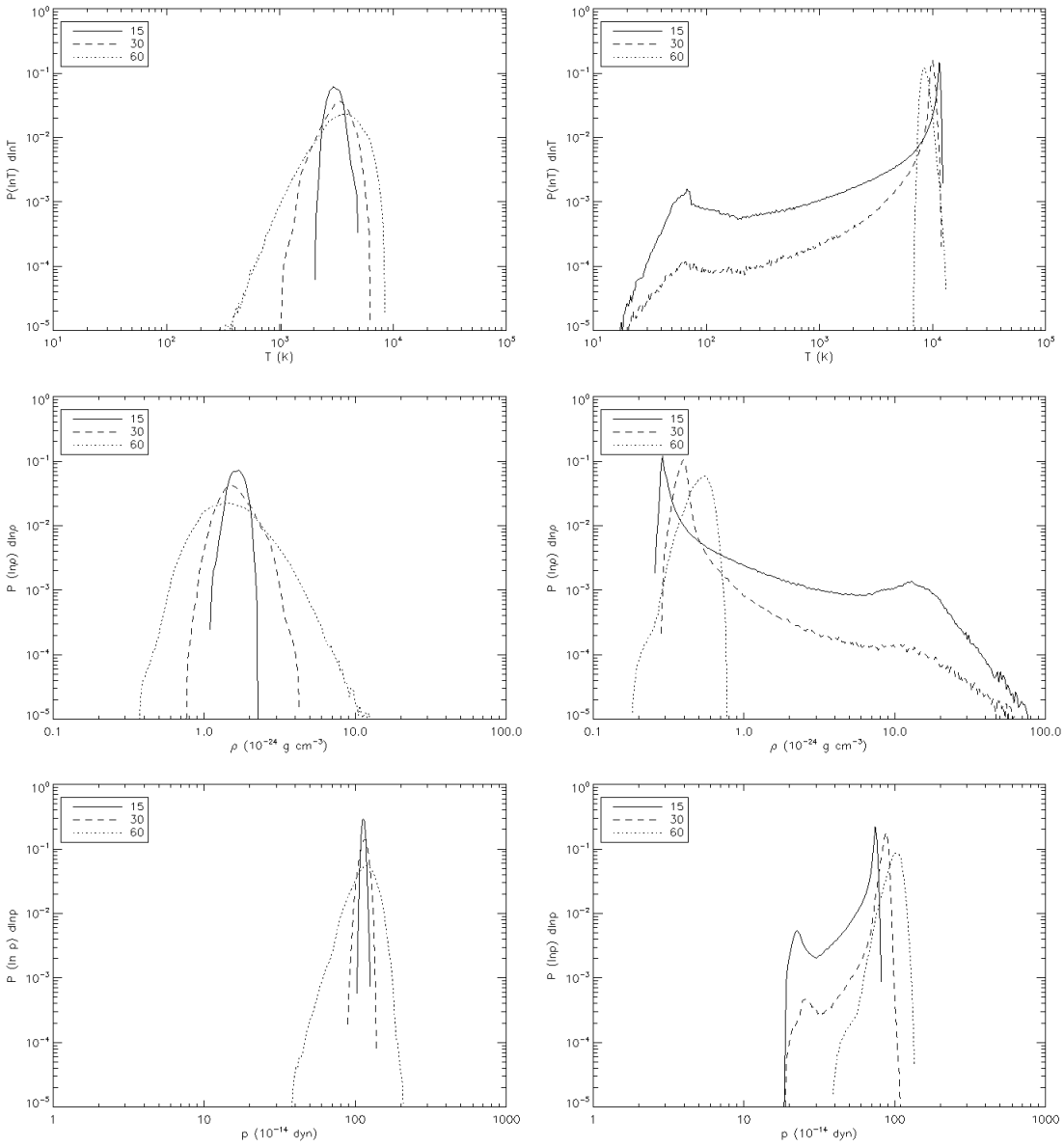

Figure 3.1: PDFs for T, ρ, and p – Probability distribution functions for temperature, density, and pressure. The left column is the stable case, and the right is the unstable case.

this regime is acting at a faster rate than TI can remove it. The forcing has the opposite effect on average values than for the stable case: stronger forcing creates higher densities and lower temperatures. The filling factor of the warm, diffuse phase of the gas is considerably larger than that for the cold, dense phase and this difference

increases with time as evidenced by the growth of the peak for lower density and higher temperature with time. With a high enough forcing, the second smaller peak for the cold, dense gas disappears almost entirely.

3.2 Magnetohydrodynamical Simulations

The MHD simulations add the effects of a magnetic field. Vazquez-Semadeni et al. (2011) found the magnetic field made condensation of the gas more difficult, especially if the magnetic pressure had a significant contribution to total pressure. The process is nonlinear, and it is possible that the TI can affect the dynamo before the magnetic field is strong enough to affect the condensation. This effect is poorly known, and part of this thesis project and the publication by Mantere et al. (2011) focuses on understanding this process.

The MHD runs consist of both helical and nonhelical runs to study the effect TI has on both the large-scale and small-scale dynamo. For the helical runs, both the stable and unstable cases are studied. In dynamo active cases, the resulting mean magnetic field has three parts: exponential decay as the initial seed field dissipates with turbulence before the magnetic field is formed, growth as the dynamo switches on and the magnetic field increases exponentially, and saturation as the system balances out to maintain a constant magnetic field and measured values become approximately constant. The evolution of the magnetic energy, the growth rate, and the saturated field strength are monitored to evaluate successful dynamo action, listed in Table (3.2). The geometrical configuration of the large-scale dynamo and generated mean components of the field are also analyzed later in this section.

3.2.1 Nonhelical Forcing

The nonhelical simulations are critical in determining whether their helical counterparts exceed the critical Rm for the small-scale dynamo with a specific value for forcing. If a small-scale dynamo cannot be generated in the nonhelical models, then it is unlikely that the small-scale dynamo is generated in the helical models as well.

Earlier work in the project by Mantere et al. (2011) with simulations with forcing equal to the helical runs for both the stable and unstable case found no small-scale dynamo with $30 < Rm < 60$. This is at odds with the work by Haugen et al. (2004),

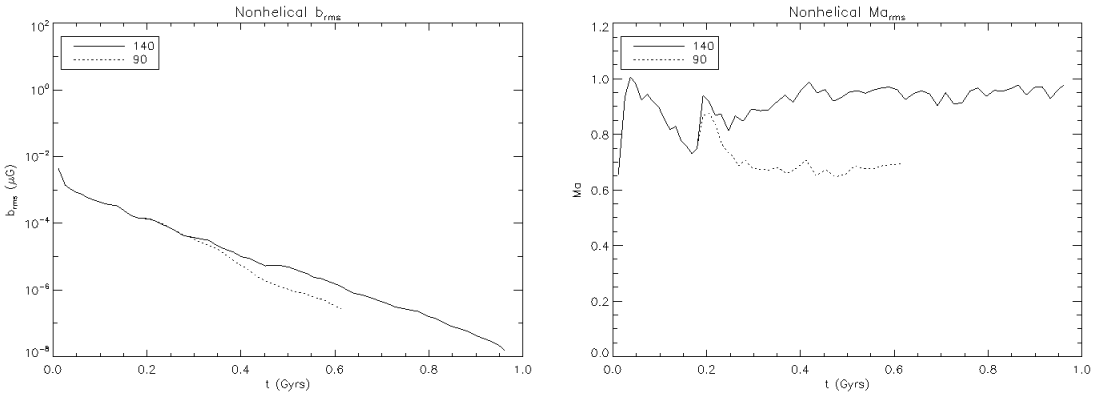

Figure 3.2: $B_{\rm rms}$ **and** $Ma_{\rm rms}$ – The rms magnetic field and rms Mach number for nonhelical runs.

who used similar setups for the isothermal case and did successfully create the small-scale dynamo. The runs specific to this thesis were an attempt to push the limits of forcing to determine if a small-scale dynamo was even possible. The setups used were based solely on ordinary viscosities and could not handle shocks, and so the limit is $Ma = 1$.

As can be seen from Figure (3.2), this limit was reached. The final forcing value for uMHDnh140 was the limit of what the code was able to handle. This corresponds to $Rm = 150$. The unstable cooling function was selected because it was more physically matched to the interstellar medium and resulted in lower Mach numbers in the helical forcing MHD simulations. No small-scale dynamo could be seen. The magnetic field died off exponentially to values too small to serve as a seed field. The limit of Ma was reached with a forcing value of 140, and so no higher forcing could be used without increasing the resolution or invoking shock-capturing numerical viscosities.

Balsara et al. (2004) investigated the small-scale dynamo in supernova-forced cases earlier and found difficulty in exciting the small-scale dynamo. In that specific case, small-scale dynamo action was driven by helicity fluctuations when supernova rates exceeded 8 times the value around the solar neighborhood. It can therefore be concluded that no small-scale dynamo can be found for this project based on the limitations of the setups. The effect TI has on the small-scale dynamo cannot be studied. However, this means that the small-scale dynamo is not likely to be present in the helical cases.

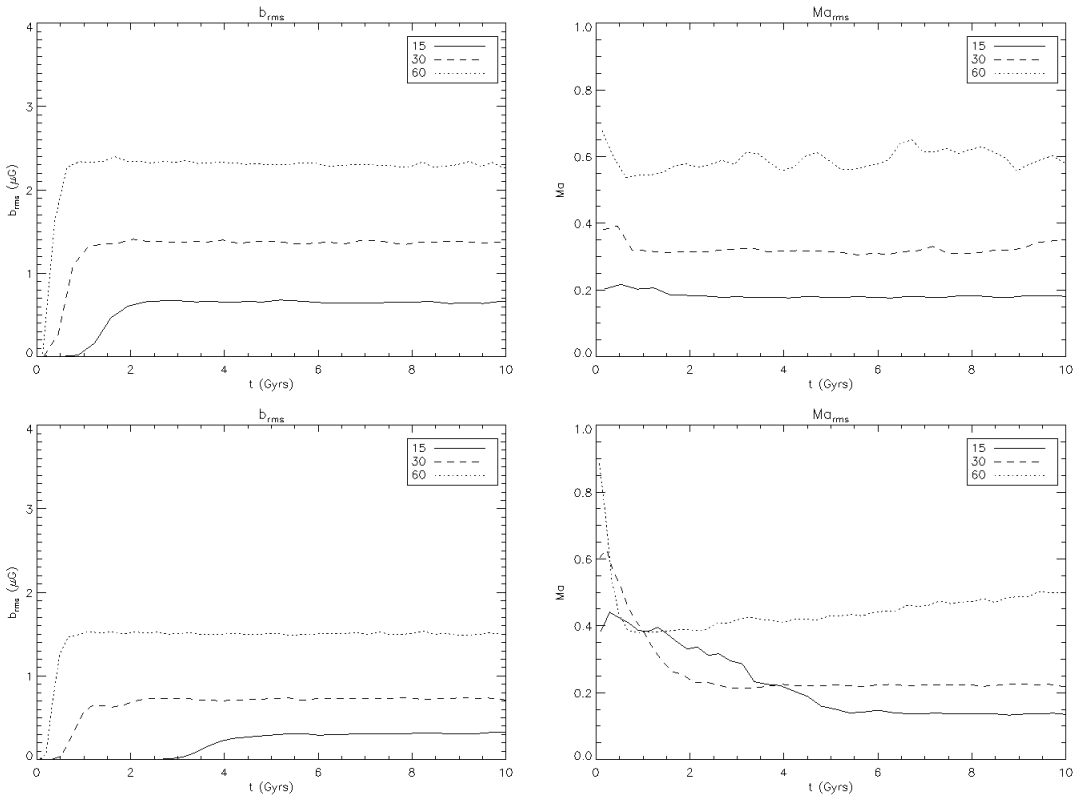

Figure 3.3: Stable and Unstable $B_{\rm rms}$ and $Ma_{\rm rms}$ – The rms magnetic field and rms Mach number for helical runs sMHD15, sMHD30, and sMHD60 (top) and uMHD15, uMHD30, and uMHD60 (bottom).

3.2.2 Helical Forcing

As discussed in Chapter 2, helical forcing without shear creates a dynamo of the α^2-type. Results from the nonhelical runs revealed that no small-scale dynamo action was likely, and so dynamo action in these models is likely to be due to the large-scale dynamo only.

From Figure (3.3), it can be seen that in the stable case, stronger forcing increases the saturated amplitude of the resulting magnetic field. The growth rate is also faster at higher forcing, and Ma becomes higher. Stronger forcing creates stronger turbulence, resulting in more energy in the system overall as well as higher gas velocities. The strongest forcing, 60, demonstrates some stronger fluctuations in Ma, indicating a sensitivity in the velocity to the forcing. The fluctuations are strong, but random.

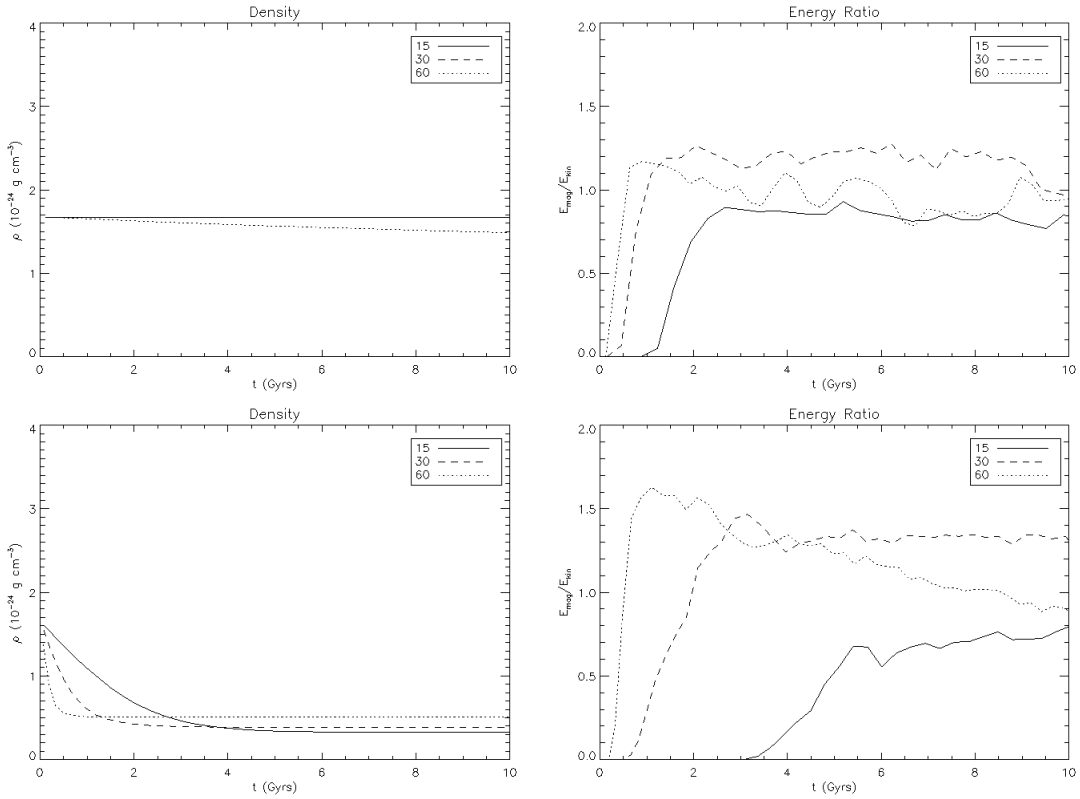

Figure 3.4: Stable and Unstable $\langle\rho\rangle$ and $E_{\rm mag}/E_{\rm kin}$ – The mean density and energy partition for helical runs sMHD15, sMHD30, and sMHD60 (top) and uMHD15, uMHD30, and uMHD60 (bottom).

Similarly to the stable case, the unstable case also sees an increase in the saturated mean field strength with increased forcing, although this value is lower than for the stable case. Growth rates follow the same tendency, with weaker forcing resulting in slower dynamo growth, which is reduced in comparison to the corresponding stable cases. Ma is overall lower than for the corresponding stable cases. However, the Mach number begins to display some interesting behavior. There is a steady increase corresponding to a steady increase in velocity after all other values have saturated. This is not due to mass loss, and means that all values taken for quantities such as $u_{\rm rms}$ depend on the time range selected for averages.

Mass loss is shown in Figure (3.4), and it can be seen that the loss is much more dramatic for the unstable case. Although the cooling functions were set to equal energy,

the difference in density changes the results so that the filling factor is unpredictable. The energy partition shows that while all the magnetic fields generated in the stable cases tend to be less than equipartition with respect to the kinetic energy, the unstable cases reach super-partition when the magnetic field has had sufficient time to saturate and the forcing was above critical.

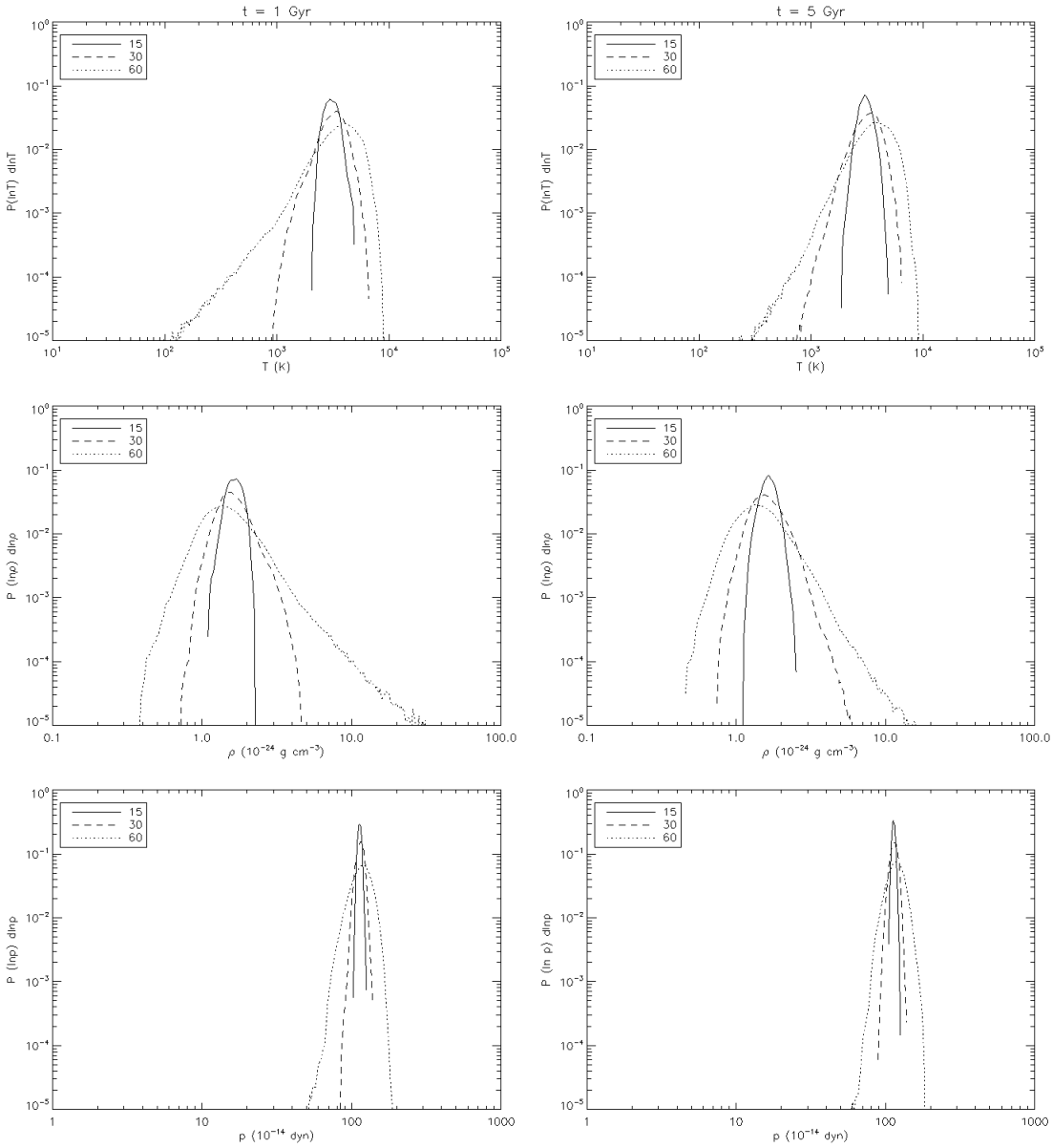

Figure 3.5: PDFs for T, ρ, and p. – Probability distribution functions for temperature, density, and pressure. The left column is taken at time slice $t = 1$ Gyr and the right at $t = 5$ Gyrs.

The PDFs are similar to the HD cases. The peak is sharper with lower forcing, and any differences between the spread and height from the HD case is minimal. The PDFs are taken at two points in time to demonstrate the changes of the gas with the

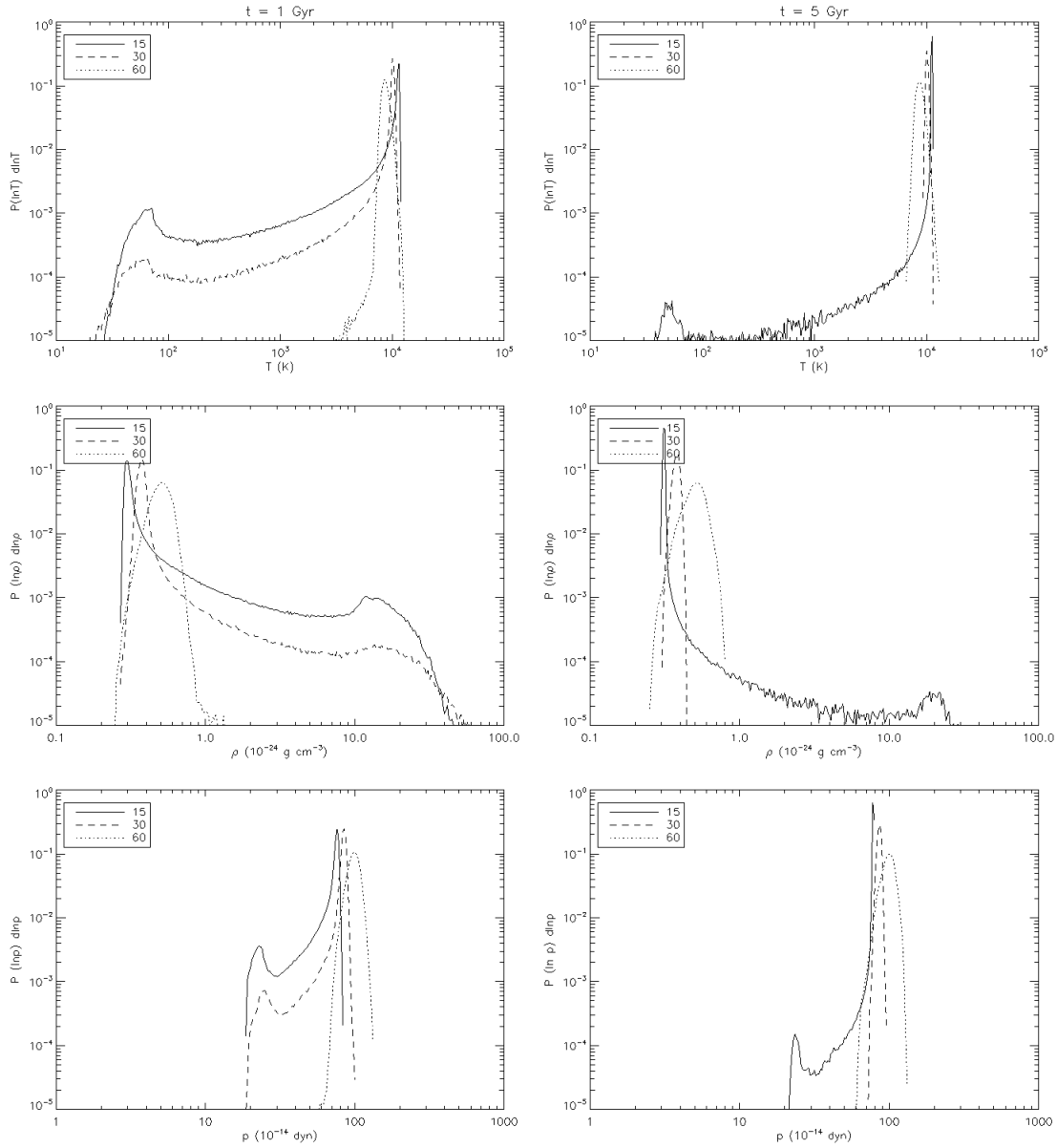

Figure 3.6: PDFs for T, ρ, and p – Probability distribution functions for temperature, density, and pressure. The left column is taken at time slice $t = 1$ Gyr and the right at $t = 5$ Gyrs.

presence of a magnetic field.

The stable case is remarkably boring over time. The distribution becomes slightly less wide, but overall the peaks keep the same values, about the same height, and the

two time slices are nearly identical. This is because the stable cooling function does not create structure; instead the gas cools around a certain stable value and remains there. There is no evidence that the magnetic field resists compression of the gas in the stable case.

The PDFs for the MHD unstable cases are more interesting. It becomes strikingly obvious that with time, gas is removed from the 'forbidden' regime and with a strong enough forcing, the second peak with the gas at the lower temperature and higher density seems to disappear almost entirely. Overall, in comparison to the stable cases, the average temperatures are higher and densities lower. Some of this may be due to the mass loss shown in Figure (3.4), but TI in general works to remove gas from the unstable region and shift it to either stable point. The PDFs for the highest forcing have very little gas in the second cold, dense state indicating the turbulence is enough to destroy any structure formed by TI over time at a faster rate than TI can create it. The magnetic field appears to have no significant effect on this destruction of structure nor does it resist the compression of values around a single peak.

3.3 Discussion

It can be seen from the results that the forcing directly affects the strength of the field created, and TI directly affects the temperatures, densities, and pressures of the gas. HD simulations can be used to isolate which effects are caused by the presence of the magnetic field upon the gas and which are due purely to TI.

3.3.1 The Magnetic Field

The magnetic field formed in the periodic box can be represented by a sinusoidal Beltrami field (i.e., $\mathbf{B} \times (\nabla \times \mathbf{B}) = 0$) that can be characterized, for example, as $\langle \mathbf{B} \rangle = (cosz, sinz, 0)$, although other directions are possible. This form of the magnetic field was found by Brandenburg (2001) to be dependent on the simulation size and geometry. This general shape of the field is independent of the forcing and Rm. To determine the mean field strength in each direction, the rms of a single component of the magnetic field is averaged over each direction within the cube. For instance, $\langle B_x \rangle_y$ is the B_x component averaged over the y-direction. The results are summed up in Table (3.3).

Model	Forcing	$\langle B_x \rangle_{y,z}$ []	$\langle B_y \rangle_{x,z}$ []	$\langle B_z \rangle_{x,y}$ []
SSf	15	0.04 ; **0.17**	0.04 ; **0.17**	0.05 ; 0.04
uMHD15	15	0.04 ; 0.04	**0.80** ; 0.03	**0.76** ; 0.03
sMHD15	15	0.04 ; 0.03	**1.57** ; 0.03	**1.57** ; 0.04
SSa	20	0.04 ; 0.04	**0.25** ; 0.02	**0.27** ; 0.04
TSa	20	0.09 ; 0.05	**0.59** ; 0.05	**0.54** ; 0.06
uMHD30	30	0.04 ; 0.06	**1.65** ; 0.03	**1.78** ; 0.06
sMHD30	30	**0.78** ; 0.08	0.66 ; 0.38	0.10 ; **0.81**
TSd	35	**0.87** ; 0.09	0.15 ; 0.17	0.15 ; **0.96**
SSb	50	**0.73** ; 0.11	0.12 ; 0.13	0.10 ; **0.75**
TSb	50	**1.21** ; 0.23	0.19 ; 0.23	0.13 ; **1.24**
uMHD60	60	**0.92** ; 0.13	0.38 ; 0.17	0.41 ; **0.87**
sMHD60	60	**1.29** ; 0.13	0.65 ; 0.12	0.57 ; **1.37**
SSc	70	0.08 ; **0.99**	0.13 ; **1.00**	0.19 ; 0.16
TSc	70	0.22 ; **1.43**	0.11 ; **1.48**	0.17 ; 0.28

Table 3.3: Results from project. Values in bold indicate the strongest direction of the magnetic field. Models for this thesis indicated in bold were taken at slice $t = 10$ Gyrs.

Although original studies by Brandenburg (2001) found the direction to be random, there appears to be a set series of ranges here based on the forcing. For $15 < f < 30$, strong components of B_y and B_z develop in the x-direction. For $30 < f < 60$, B_x and B_z develop fields in the y-direction. And finally for the strongest forcing $f = 70$, B_x and B_y develop in the z-direction. Simulations for this thesis and other simulations in the project were run using different supercomputers and so different compilers produced different random seed fields. The seed field was randomly generated once per compiler and used for each model run on that compiler.

The magnetic field can be visualized in the form of periodic boxes. The periodic boxes are the x, y, and z components of $\mathbf{B}$ taken at the boundaries. One component of $\mathbf{B}$ remains relatively structureless with random fluctuations and no periodic structure, while the other two directions form sinusoidal curves with wavenumber $k = 1$ and an approximate 90 degrees phase difference between each direction, slightly distorted by turbulence. This very clearly demonstrates the property from Brandenburg (2001) of the creation of a nearly force-free magnetic field at the largest possible scale. Even the weakest field of uMHD15 shows strong structure, even though the dynamo is not at full strength at $t = 5$ Gyrs. For comparison purposes, the scale of all periodic boxes is identical.

This structure is independent of forcing and the large-scale field is clear even without averaging. This is the "self-cleaning" process as described by Brandenburg (2001) where energy on the smaller scales is suppressed, leaving only the largest scale once the magnetic field is established. The wavenumber $k = 1$ for all models and is independent of forcing, meaning that the dynamo forms on the largest scale possible in the system. From Figure (3.7), i is apparent that the y-component is featureless for the stable cooling function and the x-component is featureless for the unstable cooling function. The unstable cooling function produces a weaker magnetic field at a slower rate, as indicated by the relatively featureless third row in Figure (3.7). However, regardless of the strength of the magnetic field, both the stable and unstable cases demonstrate a similar level of distortion due to turbulence.

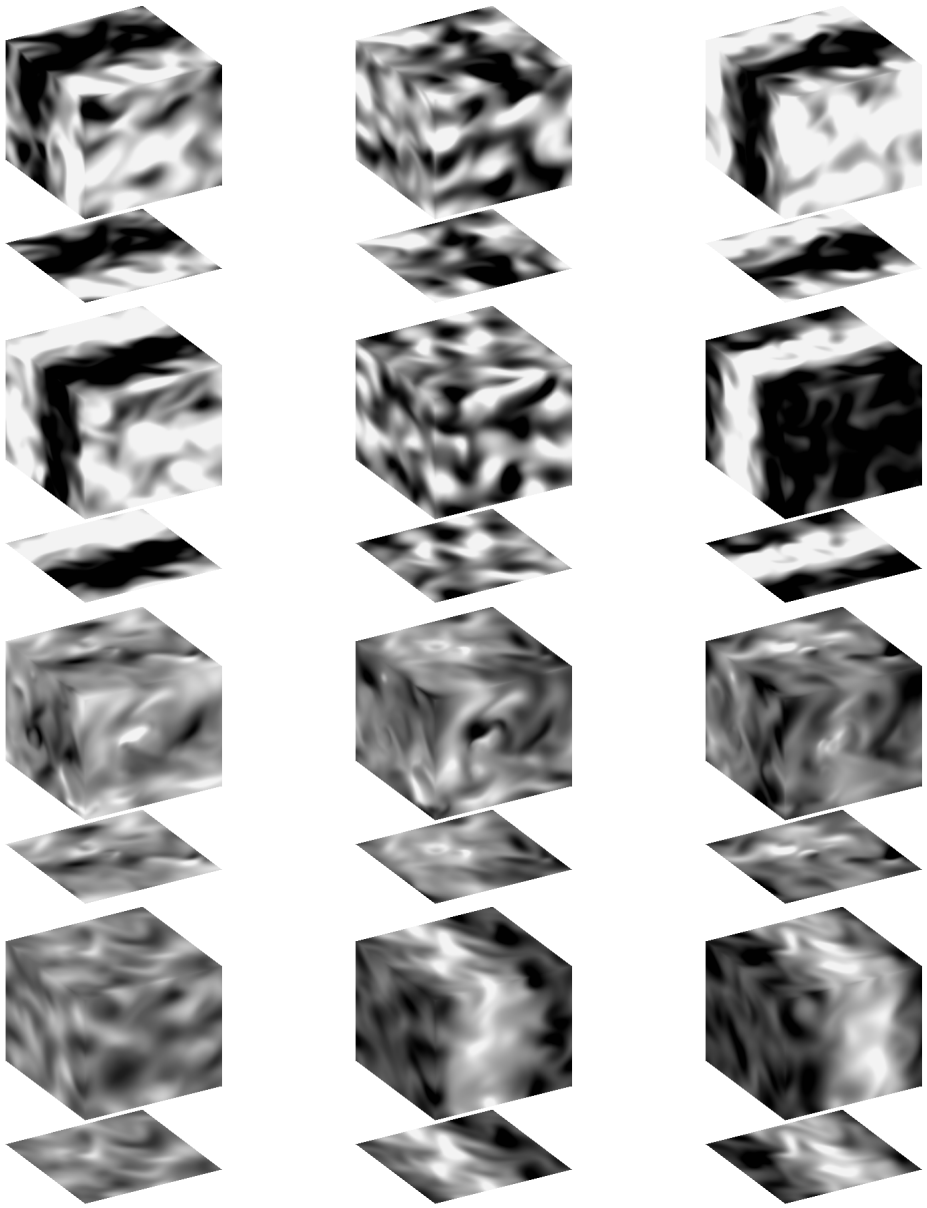

Figure 3.7: Magnetic Field Geometry – Periodic boxes of the magnetic field with time. Row 1 is sMHD30 at $t = 1$ Gyr and Row 2 is sMHD30 at $t = 5$ Gyrs. Row 3 is uMHD30 at $t = 1$ Gyr and Row 4 is uMHD30 at $t = 5$ Gyrs. The columns are B_x, B_y, and B_z from left to right. All boxes are scaled identically.

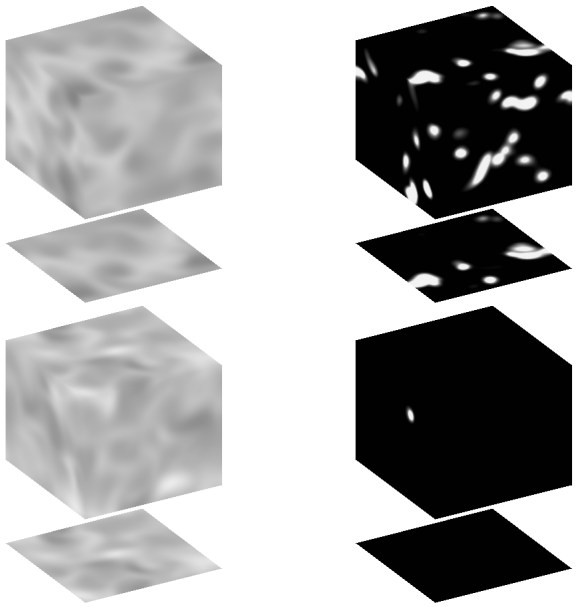

Figure 3.8: Density Evolution – Periodic boxes of the density structure. The left column is the stable case and the right column is the unstable case. The first row is the time slice $t = 1$ and the second row is later in time at $t = 5$ Gyrs. Boxes are scaled identically, and white indicates a higher density.

3.3.2 Effects of Cooling Function

The most obvious difference in the cooling function is the difference in densities created. As the histograms in the previous section demonstrated, the unstable cooling function separated the gas into two distinct phases. This created structure in the unstable case, whereas the stable case remained relatively unchanged. The structure is then destroyed with forcing over time as the gas is forced out of a stable point into the unstable regime, adding to the turbulence.

The comparison of forcing 15 for Figure (3.8) was chosen because the structure was readily visible at $t = 1$ Gyr and not yet entirely destroyed at $t = 5$, as can be seen by the clear bimodal shape of the PDFs in Figure (3.6). At higher forcing, the structure does appear to be almost completely destroyed and most of the gas becomes warm and diffuse. The same scale is chosen for both the stable and unstable cases to accentuate the difference of the resulting gas of the two cases. The stable case shows absolutely no evolution of structure, as it should, and remains approximately the same value. The

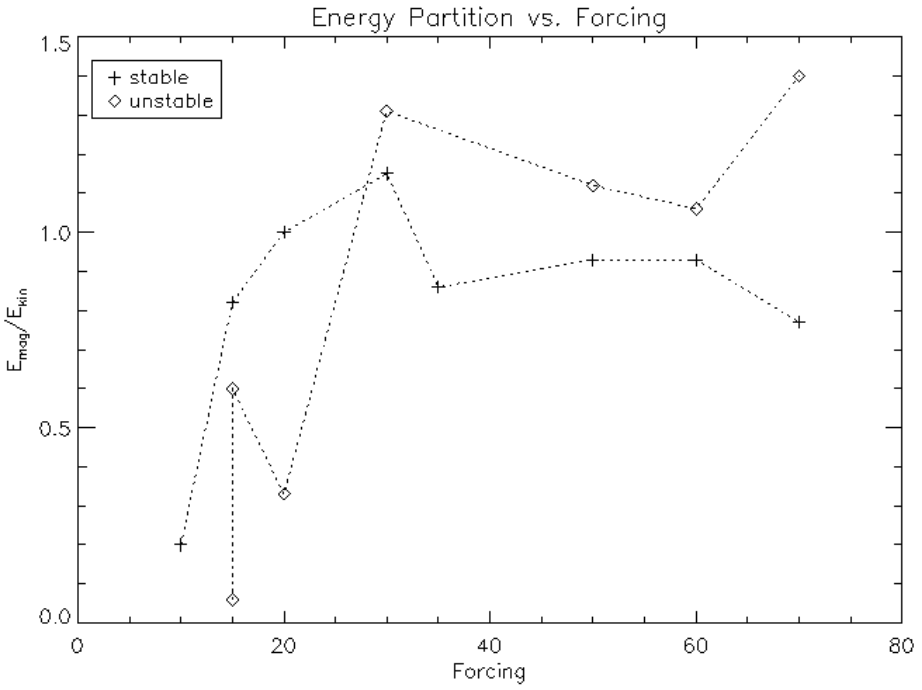

Figure 3.9: E_{mag}/E_{kin} **vs. Forcing** – Average partition energies plotted versus forcing for the stable and unstable models.

filling factor does not change for the stable case, but the ratio of cold, dense gas to warm, diffuse gas is obviously different over time in the unstable case.

The efficiency of the dynamo was judged by the total energy ratios and growth rate. Equipartition is defined to be

$$\frac{E_{mag}}{E_{kin}} = 1 \tag{3.4}$$

where E_{mag} and E_{kin} are outputted results of the forms given in equations (2.3) and (2.4) respectively and taken from the corresponding columns in Table (3.2). An efficient dynamo is saturated when half of the total kinetic energy becomes magnetic energy and the system is in equipartition. If the magnetic energy is greater than the kinetic energy, then the system is in super-partition, and if the magnetic energy less than the kinetic energy, the system is in sub-partition.

The density distribution of the runs with TI show more matter in the less dense, warmer phase. This creates a lower total kinetic energy, which is apparent in Tables (3.1) and (3.2). As can be seen from Figure (3.9), the unstable case at higher forcing

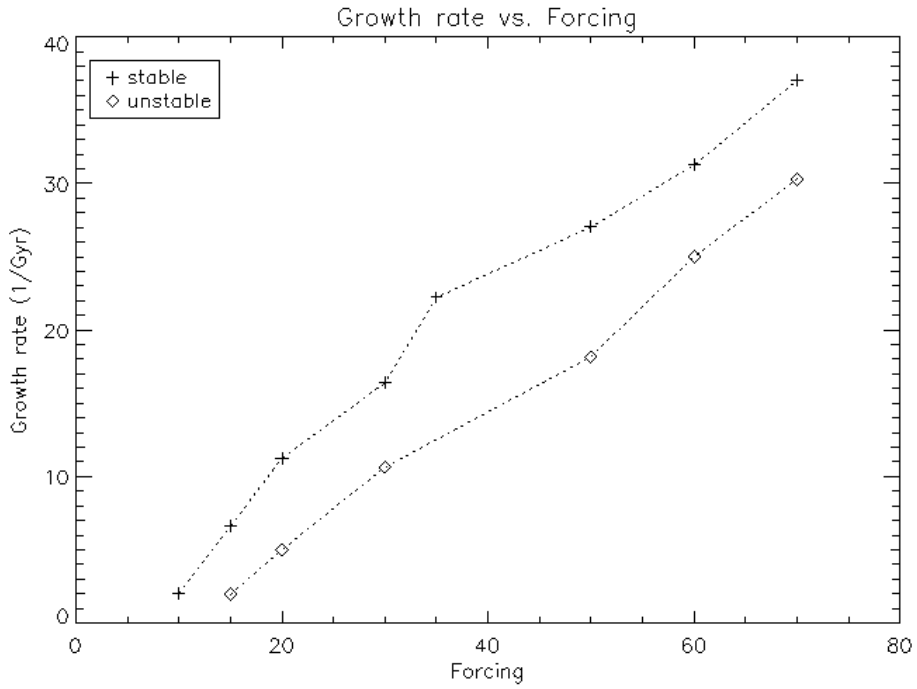

Figure 3.10: Growth Rate vs. Forcing – The growth rate in Gyrs plotted against the forcing for the stable and unstable cases.

actually goes into super-partition, implying that the dynamo creation is more efficient. At the lower forcing, $f < 30$, the unstable cases are below equipartition, and the magnetic energy is a smaller fraction of the kinetic energy.

TI can have an effect on the growth rate of the dynamo. The increase in u_{rms} from the warm, diffuse gas in turn increases the Rm, making the turbulence more vigorous than the stable case at the same forcing. To examine the growth rate for comparison, exponential growth is assumed and the rate is fitted to the form

$$\mathbf{B} = \mathbf{B}_o e^{kt} \tag{3.5}$$

where k is the growth rate, the inverse of the value indicated by the column λ_B in Table (3.2), converted into Gyrs. By using the logarithm of $\mathbf{B}$, a simple least-squares fit of a straight line to $\ln \mathbf{B}$ gave a slope of k in 1/Gyrs. For all cases except the uMHD15, this fit was fairly accurate within the time range for the growth of the dynamo. The runs are compared and then plotted against the forcing used.

As can be seen from the graph, the growth rate for the dynamo is consistently quicker for the stable cooling function. Comparing the overall field strengths of the resulting dynamos in Table 3.1, the stable cooling function results in a stronger average field strength as well. Mantere et al. (2011) found the critical Rm for dynamo action in the models to double from the stable case to the unstable case. Rm for the stable case was found to be 12-16 and in the unstable case 28-45.

3.3.3 The Small-Scale Dynamo

Unfortunately, neither model showed any activity beyond a slight delay in the decay of the magnetic field. It appears that it is not a matter of having enough forcing to create the small-scale dynamo, and that there is some further element required to create a sustained field without entering the supersonic regime. Nonhelical forcing can create a large-scale dynamo by shear or rotation, as explained previously, but in this case neither small-scale nor large-scale field is formed with just the effect of TI and random external forcing.

The Rm is theoretically large enough for a scale to form. The highest, $Rm = 150$ for the model uMHDnh140, is over double the previously estimated value of $Rm \sim 60$. The range explored was $31 < Rm < 151$ and no dynamo action was found. However, previous work in this by Haugen et al. (2004) as outlined in the previous chapter used the shock modeling and an isothermal setup, so the setups for this thesis have different properties. It is possible that the more complex properties of heating and cooling in thermodynamics alter the dependence of Rm on Ma.

The inability of the model to show dynamo action is puzzling as a higher Rm was not sufficient for dynamo action, and needs further exploration. A forcing value of 140 appears to be the limit; the code did eventually crash when random fluctuations of Ma_{rms} became supersonic for enough time-steps to cause numerical discontinuities in the calculations. Fortunately, the simulation ran for a long enough time to see the field die off to values below which the field could no longer serve as a seed.

4

Conclusions

The thesis investigated the role of TI in the interstellar medium in the context of galactic dynamos. The models run are part of a larger project that isolates TI from other possible effects to determine its importance on the efficiency of the dynamo (Mantere et al. 2011). HD simulations were run for comparison purposes to determine the effect of TI on the gas in the absence of a magnetic field, and nonhelical simulations were run in an attempt to create a small-scale dynamo.

An unstable cooling function applied to the simulations created the expected bimodal distribution for the gas, with a cold, dense phase with a small filling factor and a warm, diffuse phase, in rough pressure equilibrium. TI contributed to the general turbulence by adding its vigour, as the forcing pushed the gas into the unstable, or 'forbidden' regime. Higher forcing created a wider spread in values in probability distribution functions and added the amount of gas found in the thermally unstable regime. The stable cooling function at higher forcing produced higher temperatures and lower densities, while the unstable cooling function produced the opposite with lower temperatures and higher densities.

During this project we found a critical Rm for the large-scale dynamo creation to be between 12 – 16 for the stable case and 24 – 45 for the unstable case. All simulations run specifically for this thesis were above the critical values so that dynamo action was guaranteed. The resulting fields could be well described with sinusoidal Beltrami functions with $k = 1$ completely independent of forcing, in agreement with previous work. The prefered direction of the resulting magnetic field depended on forcing and all directions were possible.

For a certain Rm, the unstable dynamo has a slower growth rate and saturates with a lower amplitude than for the stable case. However, when the ratio of the magnetic to kinetic energies are compared, it can be observed that the unstable cooling function is capable of transferring more energy from the kinetic energy reservoir to the magnetic one than for the cases in which the stable cooling fuction is used.

The non-helical simulations with only TI did not produce a small-scale dynamo. The range of Rm was rather large, between 31 – 151. Creating and maintaining a small-scale dynamo isolated from the large-scale dynamo is still of interest. Both small-scale and large-scale fields are observable in galaxies, and so it is of importance to determine what possible phenomena control the formation of the small-scale field.

References

[1] Balsara, D., Kim, J., Mac, L., Mordecai-Mark, Mathews, G.. **Amplification of Interstellar Magnetic Fields by Supernova-driven Turbulence**. *Astrophys. J., 617, 339-49*, 2004.

[2] Beck, R.. **The Magnetic Field in M31**. *Astron. Astrophys., 106, 121-32*, 1982.

[3] Beck, R., Brandenburg, A., Moss, D., Shukurov, A., Sokoloff, D.. **Galactic Magnetism: Recent Developments and Perspectives**. *Annu. Rev. Astron. Astrophys., 34, 155-206* , 1996.

[4] Berkhuijsen, E. M., Beck, R., Hoernes, P.. **The polarized disk in M 31 at lambda 6 cm**. *Astron. Astrophys., 398, 937-48*, 1992.

[5] Brandenburg, A.. **The Inverse Cascade and Nonlinear Alpha-Effect in Simulations of Isotropic Helical Hydromagnetic Turbulence**. *Astrophys. J., 555, 824-40*, 2001.

[6] Brandenburg, A., Korpi, M. J., Mee, A. J.. **Thermal Instability in Shearing and Periodic Turbulence**. *Astrophys. J., 654, 945-54*, 2007.

[7] Brandenburg, A., Subramanian, K.. **Astrophysical Magnetic Fields and Nonlinear Dynamo Theory**. *Physics Reports, 417, 1-209*, 2005.

[8] Enqvist, K., Rez, A., Semikoz, V.. **Dirac neutrinos and primordial magnetic fields**. *Nuclear Physics, 436, 49-64*, 1995.

[9] Enqvist, K., Semikoz, V., Shukurov, A., Sokoloff, D.. **Neutrino mass and the origin of galactic magnetic fields**. *Physical Review, 48, 4557-61*, 1993.

[10] Field, G. B.. **Thermal Instability**. *Astrophys. J. 142, 531-67*, 1965.

[11] Fitt, A. J., Alexander, P.. **Magnetic Fields in Late-Type Galaxies**. *Mon. Not. R. Astron. Soc., 261, 445-52*, 1993.

[12] Frisch, U.. **Turbulence (the legacy of A. N. Kolmogorov)**. *Cambridge University Press, Cambridge*, 1995.

[13] Haugen N. E. L., Brandenburg, A., Mee, A. J.. **Mach Number Dependence of the Onset of Dynamo Action**. *Mon. Not. R. Astron. Soc. 353, 947*, 2004.

[14] Helfer, T., Thornley, M., Regan, M., Wong, T., Sheth, K., Vogel, S. Blitz, L. Bock, D.. **The BIMA Survey of Nearby Galaxies (BIMA SONG). II. The CO Data**. *Astrophys. J., Suppl. Ser., 145, 259-327*, 2003.

[15] Horellou, C., Beck, R., Berkhuijsen, E. M., Krause, M., Klein, U.. **Faraday effects in the spiral galaxy M 51**. *Astron. Astrophys., 265, 417-28*, 1992.

[16] Korpi, M.. **Interstellar turbulence and magnetic fields: the role of supernova explosions**. *PhD thesis, Univ. of Oulu*, 1999.

[17] Korpi, M., Brandenburg, A., Shukurov, A., Tuominen, I., Nordlund, Å.. **A Supernova-regulated Interstellar Medium: Simulations of the Turbulent Multiphase Medium**. *Astrophys. J. Lett., 514, L99-L102* , 1999.

[18] Koyama, H., Inutsuka, S.. **The Field Condition: a New Constraint on Spatial Resolution in Simulations of the Nonlinear Development of Thermal Instability**. *Astrophys. J. Lett., 602,L25-28* , 2004.

[19] Krause, M., Beck, R., Hummel, E.. **The Magnetic Field Structures in Two Nearby Spiral Galaxies - Part Two - the Bisymmetric Spiral Magnetic Field in M81**. *Astron. Astrophys., 217, 17-30*, 1989b.

[20] Krause, F., Rädler, K.-H.. **Mean-field magnetohydrodynamics and dynamo theory**. *Berlin: Akademie-Verlag; Oxford: Pergamon* , 1980.

REFERENCES

[21] Mantere, M., Cole, E., Fletcher, A., Shukurov, A.. **Dynamo Action in Thermally Unstable Interstellar Flows**. *Astrophys. J., arXiv:1011.4673*, 2011.

[22] Mishustin, I., Ruzmaikin, A.. **Formation of "priming" magnetic fields during the formation of protogalaxies.**. *Zh. Ehksp. Teor. Fiz., Tom 61, 441 - 444*, 1971.

[23] Parker, E. N.. **Instability of Thermal Fields**. *Astrophys. J. 117, 431*, 1953.

[24] Pohl, M.. **Magnetic Fields and the Cosmic Ray e/p Ratio. Clues from Gamma-Ray Observations of the Magellanic Clouds**. *Astron. Astrophys., Lett. 279, L17-20*, 1993.

[25] Rosen, A., Bregman, J., Norman, M.. **Hydrodynamical simulations of star-gas interactions in the interstellar medium with an external gravitational potential**. *Astrophys. J., 413, 137-49*, 1993.

[26] Ruzmaikin, A., Shukurov, D., Sokoloff, A.. **Magnetism of Spiral Galaxies**. *Nature, 336, 341-347*, 1988.

[27] Ruzmaikin, A., Sokolov, D., Shukurov, A., Beck, R.. **Magnetic field in the Andromeda Nebula inferred from polarization observations**. *Astron. Astrophys., 230, 284-92*, 1990.

[28] Rüdiger, G., Kitchatinov, L. L.. **Alpha-effect and alpha-quenching**. *Astron. Astrophys., 269, 581-588*, 1993.

[29] Sanchez-Salcedo, F. J., Vázquez-Semadeni, E., Gazol, A.. **The Nonlinear Development of the Thermal Instability in the Atomic Interstellar Medium and Its Interaction with Random Fluctuations**. *Astrophys. J., 577, 768-88*, 2002.

[30] Segalovitz, A., Shane, W. W., de Bruyn, A. G.. **Polarisation detection at radio wavelengths in three spiral galaxies**. *Nature, 264, 222-6*, 1988.

[31] Sokoloff, D., Shukurov, A., Krause, M.. **Pattern recognition of the regular magnetic field in disks of spiral galaxies**. *Astron. Astrophys., 264, 396-405*, 1992.

[32] Vázquez-Semadeni, E., Banerjee, R., Gómez, G. C., Hennebelle, P., Duffin, D., Klessen, R. S.. **Molecular cloud evolution - IV. Magnetic fields, ambipolar diffusion and the star formation efficiency**. *Mon. Not. R. Astron. Soc., arXiv:1101.3384*, 2011.

[33] Wolfire, M., McKee, C., Hollenbach, D., Tielens, A.. **The Multiphase Structure of the Galactic Halo: High-Velocity Clouds in a Hot Corona**. *Astrophys. J., 453, 673*, 1995.